공학석사학위논문

A Study on Improvement of Navigation Performance of Land Vehicle using Low Cost 2D DGPS/INS/Magnetometer Considering Gravity

중력을 고려한 저가형 2D DGPS/INS/Magnetometer 결합 차량 항법 측위 성능 향상에 관한 연구

2017년 2월

서울대학교 대학원

기계항공공학부

강 민 호

Abstract

A Study on Improvement of Navigation Performance of Land Vehicle using Low Cost 2D DGPS/INS/Magnetometer Considering Gravity

Minho Kang

School of Mechanical and Aerospace Engineering

The Graduate School

Seoul National University

In this paper, we propose an algorithm for improving the navigation positioning performance of a land vehicle using a low cost Global Positioning System (GPS) receiver, a MEMS IMU (Inertial Measurement Unit) and a magnetometer. To improve the performance of stand-alone GPS, DGPS is applied using calibration information of the reference station around the user.

In order to develop a land vehicle system, the system is simplified based on the dynamic characteristics of the land vehicle and 2D is applied. In order to minimize the error caused by the simplification process, the IMU sensor measurement modeling is improved by understanding the actual land vehicle driving characteristics, system is simplified and navigation performance is maintained. Furthermore, the addition of a magnetometer to compensate for heading information when the land vehicle stops or runs at low speed, which is

the limit of GPS/INS, is supplemented. Finally, the DGPS/INS/Magnetometer combined Extended Kalman Filter (EKF) is constructed to improve navigation performance.

To verify the EKF system combined with the DGPS/INS/Magnetometer for the land vehicle, it is verified that the simulation is able to determine the defect and improved the navigation performance, and the improvement of the navigation performance is confirmed by applying the system to the actual land vehicle.

Keywords: Land vehicle, GPS/INS Integration, Magnetometer, Kalman Filter

Student Number: 2015-20762

Table of contents

Abstract i

Table of contents iii

List of figures vi

List of tables viii

1. Introduction 1

1.1 Motivation and background 1

1.2 Research trends 3

1.3 Research content and method 4

1.4 Contribution of research results 5

2. GPS/INS/Magnetometer integrated navigation 6

2.1 GPS (Global Positioning System) 6

2.1.1 Types of GPS 7

2.1.2 GPS configuration 7

2.1.3 GPS error factor 9

2.1.4 GPS position determination method 10

2.1.5 DGPS (Differential GPS) 14

2.2 Inertial Navigation System (INS) 17

2.2.1 INS overview 17

2.2.2 Coordinate system definition 18
2.2.3 INS type 22
2.2.4 INS configuration and error factors 23
2.2.5 IMU sensor analysis 24
2.3 GPS/INS integration 27
2.3.1 GPS/INS integrated navigation overview 27
2.3.2 GPS/INS integrated navigation limit 28
2.4 Magnetometer 29
2.4.1 Magnetometer overview 29
2.4.2 Magnetometer error factor and correction method 29
2.5 GPS/INS/Magnetometer integration 31
2.5.1 GPS/INS/Magnetometer algorithm overview 31
2.5.2 2D Extended Kalman Filter for land vehicle 31
3. Simulation 38
3.1 Simulation data generation 39
3.2 2D Extended Kalman Filter algorithm for land vehicle verification 44
3.2.1 Simulation scenario 44
3.2.2 Simulation result 45
4. Actual experiment 50
4.1 System configuration 50
4.1.1 Considerations when processing actual data 50

4.1.2 Extended Kalman Filter reflecting actual data characteristics 55
4.1.3 Extended Kalman Filter Tuning 61
4.1.4 Heading alignment 63
4.2 Configure the experiment environment and scenario 64
4.3 Actual experiment result 67
4.3.1 Compare results before and after considering gravity 67
4.3.2 Analyzing the results of gravity considerations 69
5. Conclusion and future work 77
6. References 79
초 록 83

List of figures

Figure 1. GPS constellation. 6
Figure 2. GPS segment 7
Figure 3. Error source of GPS 9
Figure 4. Definition of vector 11
Figure 5. Position calculation process 13
Figure 6. Configuration of DGPS 14
Figure 7.ECI/ECEF coordinate. 18
Figure 8. Navigation frame coordinate. 19
Figure 9. Body frame coordinate and Euler angle. 20
Figure 10. Define the vector of the coordinate. 20
Figure 11. Accelerometer Allan variance. 25
Figure 12. Gyroscope Allan variance 26
Figure 13. Magnetometer error factor and calibration process 30
Figure 14. Measurement update sequence. 37
Figure 15. Magnetometer Heading 38
Figure 16. GPS Heading error configuration 40
Figure 17. GPS Heading error modeling 41
Figure 18. Simulation scenario configuration 44
Figure 19. Simulation East, North position error plot. 45
Figure 20. Simulation horizontal position error plot. 46
Figure 21. Simulation Heading error plot. 47
Figure 22. Simulation DGPS/INS bias error plot. 48
Figure 23. Simulation DGPS/INS/Magnetometer bias error plot. 48

Figure 24. Effect of accelerometer on vehicle behavior..... 51

Figure 25. Actual vehicle Roll, Pitch and dot values. 53

Figure 26. Modify DGPS Heading error model. 58

Figure 27. Magnetometer calibration process. 59

Figure 28. Magnetometer Heading error plot..... 60

Figure 29. Actual data position error plot. (for tuning)..... 61

Figure 30. 24 hour skyplot of GPS satellite. 62

Figure 31. Heading alignment..... 63

Figure 32. Visible satellite of the data collection site. 64

Figure 33. Place of experiment and user. 65

Figure 34. System configuration 65

Figure 35. Data collection scenario 66

Figure 36. Comparison of horizontal position error plot before and after considering gravity at all corner..... 68

Figure 37. East, North position error plot. 69

Figure 38. Horizontal position error plot. 70

Figure 39. Heading error plot..... 71

Figure 40. Bias error plot..... 72

Figure 41. Position error plot. (waiting section)..... 73

Figure 42. Heading error plot. (waiting section) 73

Figure 43. Position error plot. (driving section)..... 75

Figure 44. Heading error plot. (driving section)..... 75

List of tables

Table 1. IMU sensor classification by performance 24

Table 2. Accelerometer Velocity Random Walk 25

Table 3. Gyroscope Angular Random Walk 26

Table 4. Compare of GPS and INS 28

Table 5. Simulation East position error result. 45

Table 6. Simulation North position error result. 46

Table 7. Simulation horizontal position error result. 46

Table 8. Actual DGPS data based horizontal position error. 57

Table 9. Actual DGPS data based velocity error 57

Table 10. DGPS position, velocity error tuning result. 62

Table 11. Comparison of horizontal position error rms result before and after considering gravity at all corner 68

Table 12. East position error rms result. 69

Table 13. North position error rms result. 69

Table 14. Horizontal position error rms. 70

Table 15. Horizontal position error rms result. (waiting section) 73

Table 16. Heading error rms result. (waiting section) 74

Table 17. Position error rms result. (driving section) 75

Table 18. Heading error rms result. (driving section) 75

1. Introduction

1.1 Motivation and background

GPS, which is a representative satellite navigation system (GNSS, Global Navigation Satellite System), is widely used in several fields with the accuracy of location and accuracy of location and accuracy of the stand-alone navigation system to several meters in open environment.

Navigation systems based on GPS navigation have already been used on navigation of vehicles, and its application range is gradually expanding. Furthermore, the accuracy of navigation information becomes more important in the implementation of future-oriented safety and comfort devices such as lane departure alarms, collision alert devices and autonomous navigation devices, which are advanced safety aids for vehicles. However, due to various error factors and environmental constraints, the stand-alone GPS solution does not meet the navigation accuracy required for the implementation of the above mentioned devices.

Inertial Navigation System (INS) was developed by MIT in the early 1950s. It is a navigation system that has been put into practical use since the 1960s. Assuming initial position, acceleration is measured and integrated to estimate the speed and position of the vehicle. Due to the characteristics of the integral, there are few errors within a short period of time, but there is a disadvantage

that the errors accumulate as time passes. However, the inertial navigation system is not affected by the external environment and does not require the assistance of other devices. In addition, it is more suitable for use in high mobility vehicles such as airplanes and car because it provides a higher level of navigation solution than satellite navigation systems.

By combining GPS and INS, the advantages and disadvantages of each can be complemented, resulting in a synergy effect. As a result, it is possible to achieve a fast navigation speed while having constant accuracy.

In this study, to improve the GPS/INS integrated navigation algorithm which is generally applied to the car navigation, we used DGPS (Differential GPS) which improves the position accuracy by using the correction information of the stand-alone GPS relative to the peripheral reference station. In addition to reducing the amount of computation by simplifying 2D in consideration of the characteristics of the vehicle, an Extended Kalman Filter was constructed by canceling the error due to the gravity caused by the 2D assumption through IMU sensor modeling. Furthermore, when the vehicle is stopped in the GPS/INS combined navigation, attitude information is easy to diverge, and a magnetometer is additionally installed to prevent and compensate for this.

Finally, DGPS/INS/Magnetometer integrated navigation algorithm was constructed. Simulation is used to determine whether there was an error in the algorithm. Lastly, the performance is verified by analyzing the results through actual experiments.

1.2 Research trends

In recent years, researches on precise positioning for automobiles have been actively conducted by automobile manufacturers and academies in order to apply unmanned automobiles and advanced safety assisting devices to automobile. Although the position of the automobile is detected using the GNSS, which is the most used positioning system, GNSS alone cannot achieve the positioning accuracy and has a low output rate of about 1Hz. It is not enough to ensure safety. Therefore, in addition to GNSS, it is also actively researching precision positioning technology that improves positioning accuracy by combining inertial navigation sensors such as odometer and IMU, or matching information detected by image and Lidar sensor with landmark and lane information recorded in precision map [1], [2], [3].

In the latter case, since the price of the sensor is very high, there are still many limitations to be put into practical use. In the former case, however, inertial navigation sensors are more advantageous for practical use because relatively low-cost sensors are widely used.

Recent studies have shown that many researches have been conducted on car navigation systems that combine GPS and INS [4], [5], [6]. The GPS-RTK/INS combined with the GPS-RTK, which is much better than the stand-alone GPS position accuracy and the GPS/IMU combined system [7], GPS/IMU combined system is used to correct position and attitude through IMU sensor when GPS signal is outage [8], [9], [10]. Research has been carried out on navigation using only 1-axis gyroscope and 2-axis accelerometer for cost reduction in research and GPS/IMU combination [11].

In addition, by improving the performance of GPS/DR(Dead Reckoning) integrated navigation system by changing the system state equation and measurement equation according to the GPS navigation solution and the movement of the vehicle [12]. A Study on relative position estimation of multiple vehicles using GPS/INS and wireless communication module [13], [14]. Using GPS/INS and wireless communication module Zero-Velocity Update (ZUPT) has been studies as an algorithm approach to study the relative position estimation of multiple vehicles and to improve the estimation performance of navigation solutions [15]. In addition, based on the GPS / INS combination, there is research to further improve the navigation solution by adding a vehicle's odometer, wheel sensor [16], [17], [18] or adding a magnetometer [19], [20], [21], [22]. In addition, studies are being conducted to combine Vision sensor, Radar [23] and Extended Digital Map.

1.3 Research content and method

In this paper, 2D DGPS/INS/Magnetometer combined navigation system for vehicle is constructed. Considering the characteristics of the vehicle, it is possible to apply 2D to ignore the effect of altitude and to reduce the computational complexity of navigation. In addition, the number of IMU sensors can reduce to 1-axis gyroscope and 2-axis accelerometer. However, considering 2D, the error due to gravity in the IMU sensor, which can reduce errors through new modeling. GPS/INS navigation also has the disadvantage that it cannot update the vehicle’s attitude information when the vehicle is stop.

It is designed so that attitude information can always be obtained regardless of the state of the vehicle by adding a magnetometer.

The system is verified by simulating the system and finally the simulation of the system is finally verified by conducting actual vehicle experiments through post-processing.

1.4 Contribution of research results

GPS/INS navigation system used for navigation of a vehicle is generally determined by considering the 3D navigation solution. However, this study considers 2D DGPS/INS/Magnetometer navigation system considering the characteristics of the vehicle and tried to reduce the error by applying the DGPS using the reference station of correction information. Also, by reducing the number of IMU sensors to 1-axis gyroscope and 2-axis accelerometer, it is possible to reduce the cost. In consideration of 2D, IMU sensor should take into account the error due to gravity. Lastly, it is possible to contribute to stability improvement by providing stable attitude information for all sections by supplementing the divergence of attitude information when vehicle stops, which is a disadvantage of GPS/INS, with a magnetometer.

Finally, we have developed a system that can maintain navigation performance while reducing cost compared with general GPS / INS system. This system can provide reliable navigation solution and it will be useful for development of unmanned vehicle and advanced safety device in the future.

2. GPS/INS/Magnetometer integrated navigation

2.1 GPS (Global Positioning System)

GPS [24], [25], [26], [27], [28] began development in 1973 as part of the NAVSTAR program of the US Department of Defense and launched GPS satellites for the first time in 1978. By 1995, GPS is establish to start Full Operation Capability (FOC). As it started to develop for military use, it did not open to the private sector at first. However, as the interest in navigation increased due to the accident of KAL007 in 1983, GPS began to open to the private sector. However, only part of it opened and it included intentional noise (Selective Availability, SA) so that accurate location information could not obtained when it used in the private sector. As a result, accuracy of civilian positioning accuracy was as low as 30~100m, but in 2000, President Clinton of the United States announced the cancellation of the deliberate error, and the accuracy of the civilian positioning accuracy became less than 30m.

Figure 1. GPS constellation.

2.1.1 Types of GPS

There are three types of GPS. Stand-alone GPS with position accuracy of several tens of meters, DGPS (Differential GPS) with position accuracy of several meters, and CDGPS (Carrier phase Differential GPS) with position accuracy of centimeter class. In this study, we will use DGPS with error of several meters.

2.1.2 GPS configuration

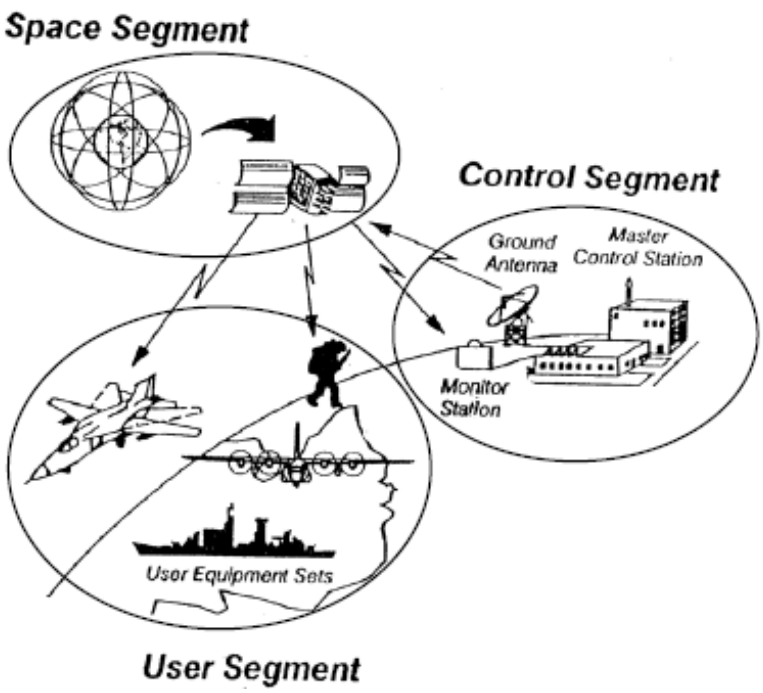

Figure 2. GPS segment

① **Space segment**

Space segment is composed of GPS satellites that serve as a carrier wave to users. Each satellite consists of 21 satellites and 3 pre-satellite arranged on 6 orbits with an inclination angle of four. GPS satellite deployed at altitudes of 20,183 to 20,187 meters, and revolve around the earth once every 11 hours 58 minutes. Each GPS satellite is equipped with an atomic clock to provide highly precise time information with a precision of about one second per 36,000 years.

② **Control segment**

Control segment consists of one main control station in Colorado, five monitoring station widely distributed around the world, and three ground control station. Main control station is responsible for commanding the GPS satellites, such as modifying the satellite's orbit and determining the operation of the pre-satellite. Five monitoring stations are equipped with atomic clocks at very precisely measured positions, checking signals of all GPS satellites, tracking orbits, and correcting error by observing the propagation delay caused by the ionosphere and the convection layer. Three ground control stations are equipped with an uplink antenna that can transmit information to the satellite, such as a clock correction value, orbit correction value, and a message to transmit to the user.

③ **User segment**

User segment refers to all equipment that receives signals transmitted from GPS satellites and uses them for navigation, geodesic, time measurement and synchronization, and so on.

2.1.3 GPS error factor

Pseudorange, which is one of the measurements provided by the GPS receiver, is a value corresponding to the distance from the GPS signal to the point of arrival at the user's receiver.

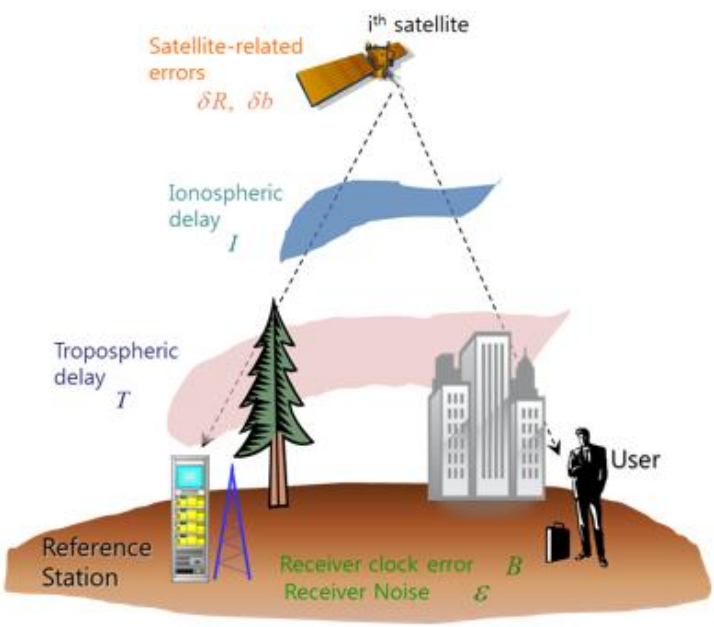

$$\rho^i = d^i - b^i + B + \delta R^i + I^i + T^i + \varepsilon$$

Figure 3. Error source of GPS

Pseudorange includes several errors, which can divide into three types: satellite related errors, atmospheric related errors, and user receiver related errors. Because of this error, the distance between the actual satellite and the user is different, which is called a pseudorange.

Among the above three errors, the satellite related errors are the satellite position errors and the satellite clock errors, and the air related errors are the ionosphere and convective delay errors that occur when the GPS signals through the ionosphere and the convection layer. The user receiver related error is the receiver clock error and noise included in the user receiver. In case of stand-alone GPS, position error of several meters to several tens of meters occurs due to such error factors.

2.1.4 GPS position determination method

Stand-alone GPS navigation equation that calculates the user's position and the receiver's clock error using pseudorange measurement is derived as follows.

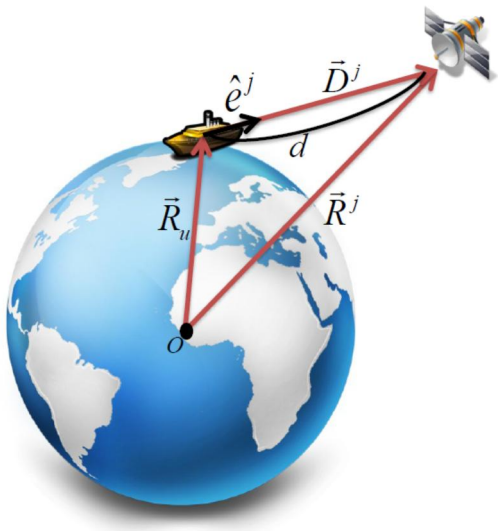

Figure 4. Definition of vector

If the position vector of the user is $\vec{R}_u$, the position vector of the j-th satellite is $\vec{R}^j$, and the vector from the user position to the j-th satellite is $\vec{D}^j$, then the relation of (2.1) is established. This is shown in Figure 4.

$$\vec{R}^j = \vec{R}_u + \vec{D}^j \tag{2.1}$$

Let $\hat{e}^j$ be the unit vector from the user location to the j-th satellite, and the distance d^j between the user and the j-th satellite can be expressed as (2.2).

$$\begin{aligned} d^j &= \left|\vec{D}^j\right| = \vec{D}^j \cdot \hat{e}^j \\ &= \left(\vec{R}^j - \vec{R}_u\right) \cdot \hat{e}^j \end{aligned} \tag{2.2}$$

Pseudorange measurements of the j-th satellite can be expressed as (2.3) by simplifying the distance between the user and the satellite and the receiver clock error.

$$\begin{aligned}\rho^j &= d^j + B \\ &= \left(\vec{R}^j - \vec{R}_u\right)\cdot \hat{e}^j + B\end{aligned} \tag{2.3}$$

In addition, the form of expression is changed to (2.4).

$$\hat{e}^j \cdot \vec{R}_u - B = \vec{R}^j \cdot \hat{e}^j - \rho^j \tag{2.4}$$

If (2.4) is expressed in a matrix form for all visible satellites (j=1,2,…,m).

$$\begin{bmatrix} \hat{e}^1 & -1 \\ \hat{e}^2 & -1 \\ \vdots & \vdots \\ \hat{e}^m & -1 \end{bmatrix} \begin{bmatrix} \vec{R}_u \\ B \end{bmatrix} = \begin{bmatrix} \vec{R}^1 \cdot \hat{e}^1 - \rho^1 \\ \vec{R}^2 \cdot \hat{e}^2 - \rho^2 \\ \vdots \\ \vec{R}^m \cdot \hat{e}^m - \rho^m \end{bmatrix} \tag{2.5}$$
$$\Rightarrow H \cdot \vec{x} = \vec{z}$$

Since (2.5) has 4 unknowns (3 user positions, 1 receiver clock error), we can obtain the solution by least square method (2.6) if there are more than 4 visible satellites.

$$\vec{x} = \left(H^T H\right)^{-1} \cdot H^T \cdot \vec{z} \tag{2.6}$$

In this case, position of the satellite can be calculated using ephemeris, and the user's position is calculated repeatedly, assuming the initial value, until the position solution of the user converges to a certain level or less.

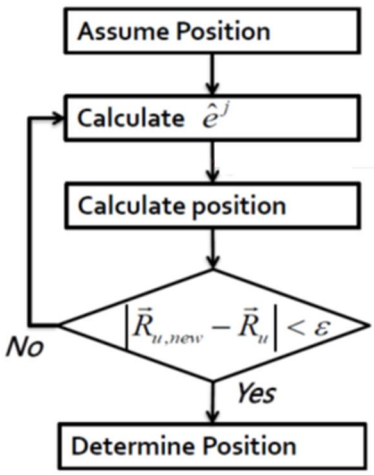

Figure 5. Position calculation process

Actual pseudorange measurements are described in (2.7), which is different from (2.3) and includes several errors.

$$\rho^j = d^j - b^j + B + \delta R^j + I^j + T^j + \varepsilon \qquad (2.7)$$

For stand-alone users, the satellite clock error (b^j) can be removed from the broadcasting ephemeris among the various error factors in (2.7), and the ionosphere delay error (I^j) and the convective layer delay error (T^j) are usually removed through a model.

The satellite clock error and the ionosphere and convective delay error values provided by the broadcasting ephemeris are $\hat{b}^j, \hat{I}^j$, and $\hat{T}^j$, respectively, and compensated to obtain the compensated pseudorange measurement as (2.8). we use this to calculate the user's position as in (2.5).

At this time, as shown in (2.8), the remaining uncorrected satellite position error, satellite clock, ionosphere delay and residual error after correction of the convective layer delay error cause the error of the user position.

$$\begin{aligned}\hat{\rho}^j &= \rho^j + \hat{b}^j - \hat{I}^j - \hat{T}^j \\ &= d^j - \left(b^j - \hat{b}^j\right) + B + \delta R^j + \left(I^j - \hat{I}^j\right) + \left(T^j - \hat{T}^j\right) + \varepsilon \\ &= d^j - \delta b^j + B + \delta R^j + \delta I^j + \delta T^j + \varepsilon\end{aligned} \tag{2.8}$$

2.1.5 DGPS (Differential GPS)

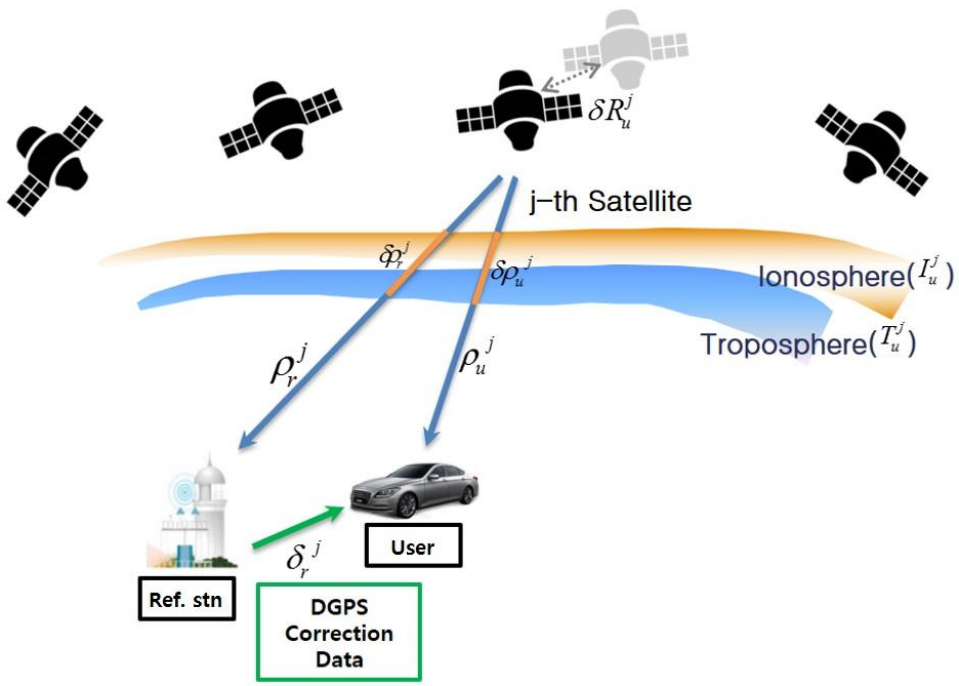

Figure 6. Configuration of DGPS

Among the error factors of GPS, the ionosphere layer delay error ($I_u{}^j$), convective layer delay error ($T_u{}^j$), satellite position error ($\delta R_u{}^j$), and satellite clock error (b^j) do not change much according to the region, so users within the same area range (within about 200 km) have common error. Therefore, the reference station which knows the exact position receives the GPS signal to generate the correction information (Pseudo Range Correction, PRC), and the user around the reference station uses it to correct the error of the GPS signal received by the reference station. It is then possible to improve position accuracy and is called DGPS.

The method of calculating the navigation solution of DGPS is as follows. First, if the pseudorange measurement from the j-th satellite of the reference station is defined as $\rho_r{}^j$, it can be expressed as (2.9).

$$\rho_r^j = d_r^j - b^j + B_r + \delta R_r^j + I_r^j + T_r^j + \varepsilon_r \tag{2.9}$$

From this, if the pseudorange correction information provided by the reference station is defined as $\delta_r{}^j$, it can be defined as (2.10).

$$\begin{aligned} \delta_r^j &\equiv \rho_r^j - d_r{}^j \\ &= -\delta b^j + B_r + \delta R_r^j + I_r^j + T_r^j + \varepsilon_r \end{aligned} \tag{2.10}$$

Similarly, if the user's pseudorange measurement from the j-th satellite is defined as $\rho_u{}^j$, it can be expressed as (2.11).

$$\rho_u^j = d_u^j - b^j + B_u + \delta R_u^j + I_u^j + T_u^j + \varepsilon_u \tag{2.11}$$

At this time, if the user's pseudorange measurement is corrected using the correction information of (2.10), the form becomes (2.12).

$$\begin{aligned}\tilde{\rho}_u^j &= d_u^j - b^j + B_u + \delta R_u^j + I_u^j + T_u^j + \varepsilon_u - \delta_r{}^j \\ &= d_u^j + (B_u - B_r) + (\delta R_u^j - \delta R_r^j) + (I_u^j - I_r^j) + (T_u^j - T_r^j) + (\varepsilon_u - \varepsilon_r) \\ &= d_u^j + \Delta B + (\delta R_u^j - \delta R_r^j) + (I_u^j - I_r^j) + (T_u^j - T_r^j) + (\varepsilon_u - \varepsilon_r) \\ &\cong d_u^j + \Delta B \\ &= (\bar{R}^j - \bar{R}_u) \cdot \hat{e}_u{}^j + \Delta B\end{aligned} \tag{2.12}$$

If (2.13) is expressed in a matrix form for all visible satellites (j=1,2, ,…,m).

$$\begin{bmatrix} \hat{e}^1 & -1 \\ \hat{e}^2 & -1 \\ \vdots & \vdots \\ \hat{e}^m & -1 \end{bmatrix} \begin{bmatrix} \vec{R}_u \\ \Delta B \end{bmatrix} = \begin{bmatrix} \vec{R}^1 \cdot \hat{e}^1 - \tilde{\rho}^1 \\ \vec{R}^2 \cdot \hat{e}^2 - \tilde{\rho}^2 \\ \vdots \\ \vec{R}^m \cdot \hat{e}^m - \tilde{\rho}^m \end{bmatrix} \tag{2.13}$$

$$\Rightarrow H \cdot \vec{x} = \vec{z}$$

Since (2.13) has 4 unknowns (3 user positions, 1 receiver clock error), we can obtain the solution by least square method (2.14) if there are more than 4 visible satellites.

$$\vec{x} = \left(H^T H\right)^{-1} \cdot H^T \cdot \vec{z} \tag{2.14}$$

2.2 Inertial Navigation System (INS)

2.2.1 INS overview

INS was developed at MIT in the early 1950s and is a navigation system that has been put into practical use since the 1960s. If the initial position information is known, the position and velocity of the vehicle can be estimated by performing integration through acceleration measurement. Since the navigation solution provided by the inertial navigation system is an integral solution, it is possible to obtain a navigation solution in which noises of a high frequency component are removed and an accurate navigation solution can be obtained in a short time. In addition, because it carries out its own navigation without using other external devices, it provides continuous navigation solution without being influenced by external environmental factors. also the navigation output is very high, ranging from 10Hz to 10kHz, which can be used to navigate and control the high mobility vehicle. However, there is a disadvantage that bias solution, which is a low-frequency component, diverges over time.

2.2.2 Coordinate system definition

2.2.2.1 Earth Centered Inertial (ECI)

The ECI coordinate is only coordinate to which Newton's 2nd law can be applied, and the direction of the coordinate is fixed for the star. As shown in Figure 7, the origin defines the center of the earth, x-axis is the vernal equinox, and z-axis is earth's axis.

2.2.2.2 Earth Centered Earth Fixed (ECEF)

It is a coordinate system in which the coordinates are fixed on the earth and rotated together with the earth in consideration of the rotation of the earth. The ECEF coordinate coincides with the ECI coordinate and is rotated by the rotation speed of the earth in the z-axis direction. It is a coordinate that is also used for commonly used GPS.

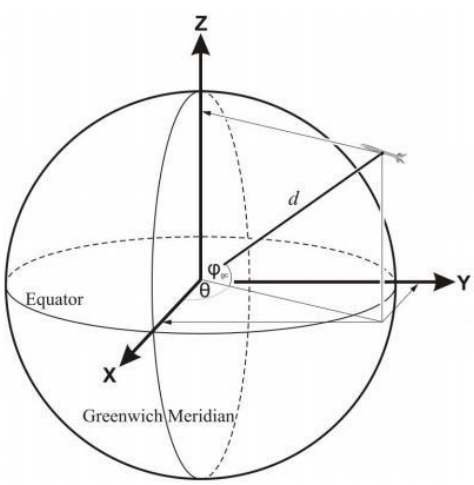

Figure 7.ECI/ECEF coordinate.

2.2.2.3 Navigation frame

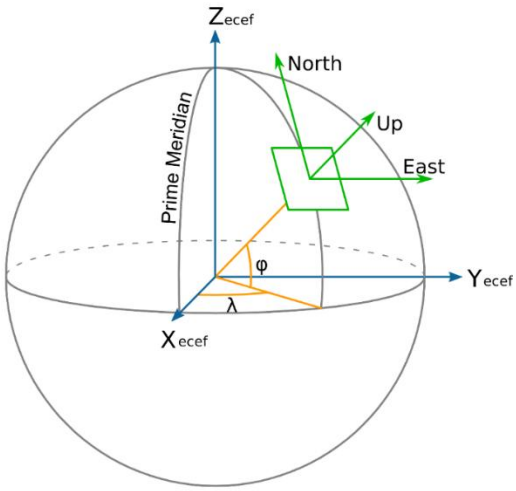

Figure 8. Navigation frame coordinate.

Navigation frame is a coordinate system in which the origin is at the position (latitude, longitude, altitude) of the vehicle, and coordinate axes are generally represented by ENU coordinates as shown in Figure 8.

North axis is orthogonal projection to the north of the local-level plane of the earth's rotation vector, up axis is the direction perpendicular to the earth ellipsoid, and east axis is defined as the east direction perpendicular to north and up axes.

Similar to the ENU coordinates, NED coordinate is often used. NED coordinate has almost the same definition as the ENU coordinate and only the definition in the down direction. Down is a vector in the direction of the center of the earth opposite to the up direction.

2.2.2.4 Body frame

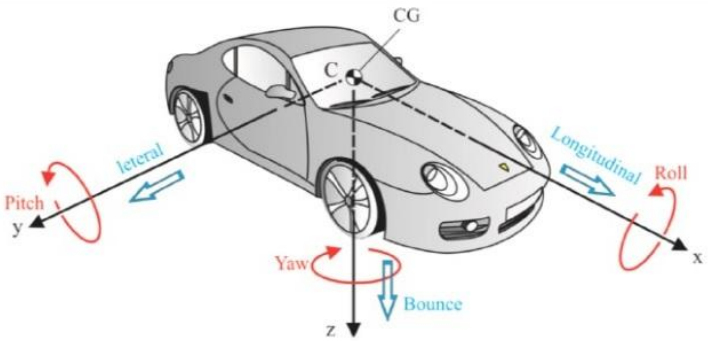

Figure 9. Body frame coordinate and Euler angle.

In the body frame, origin is at the center of the vehicle, and x-axis is set to the front of the vehicle, y-axis to the right, and z-axis to the bottom of the vehicle. Generally, when attaching a sensor to a vehicle, it is common to attach the sensor axis so that it coincides with the body frame.

2.2.2.5 Coordinate transformation

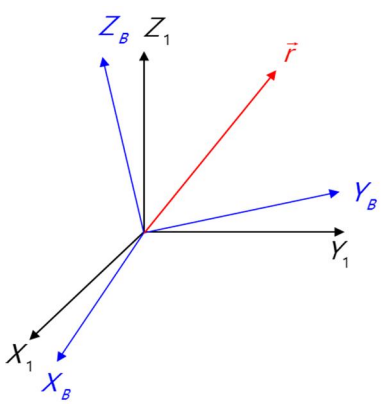

Figure 10. Define the vector of the coordinate.

In Figure 10, define the body frame of the vehicle as (X_B, Y_B, Z_B) and define another arbitrary coordinate as (X_1, Y_1, Z_1). At this time, when arbitrary r is expressed for each coordinate, it can be expressed as (2.15).

$$\begin{aligned} r^B &= \left[r_{Bx},\ r_{By},\ r_{Bz} \right]^T \\ r^1 &= \left[r_{1x},\ r_{1y},\ r_{1z} \right]^T \end{aligned} \tag{2.15}$$

Transformation relation between two vectors are defined as (2.16), and C_B^1 is defined as a body-frame to 1-frame conversion matrix (Direction Cosine Matrix, DCM).

$$r^1 = C_B^1 \cdot r^B \tag{2.16}$$

In the three-dimensional space, the coordinate can transform through three rotations using three angles. In this case, the commonly used angle is the Euler angle defined in Figure 9 and defined as Roll (ϕ), Pitch (θ), and Raw (ψ). The coordinate transformation procedure using the Euler angle proceeds as follows.

i) Rotate Yaw (ψ) about Z_1 axis. (Coordinates after rotation: X_2, Y_2, Z_2)

ii) Rotate Pitch (θ) about Y_2 axis. (Coordinates after rotation: X_3, Y_3, Z_3)

iii) Rotate Roll (ϕ) about X_3 axis. (Coordinates after rotation: X_B, Y_B, Z_B)

If this process is expressed in the form of a coordinate transformation matrix, it can be expressed by (2.17).

$$C_1^B = R(1,\phi) \cdot R(2,\theta) \cdot R(3,\psi) \tag{2.17}$$

$$\textit{where, } R(3,\psi) = \begin{bmatrix} \cos\psi & \sin\psi & 0 \\ -\sin\psi & \cos\psi & 0 \\ 0 & 0 & 1 \end{bmatrix}$$

$$R(2,\theta) = \begin{bmatrix} \cos\theta & 0 & -\sin\theta \\ 0 & 1 & 0 \\ \sin\theta & 0 & \cos\theta \end{bmatrix}$$

$$R(1,\phi) = \begin{bmatrix} 1 & 0 & 0 \\ 0 & \cos\phi & \sin\phi \\ 0 & -\sin\phi & \cos\phi \end{bmatrix}$$

2.2.3 INS type

INS is classified into gimbaled system and strapdown system [29]. In the gimbaled system, the accelerometer and gyroscope are mounted on the gimbals, and the gimbals are controlled so that navigation coordinate can always be maintained even when vehicle moves. Therefore, there is no need for coordinate conversion and the accuracy is very high, but it is mainly used for military purpose because it is expensive and heavy.

Strapdown system has no gimbals and is equipped with an INS on the axis of vehicle. Therefore, it is used in many fields because it is light and structurally simple. However, since the coordinate transformation to the navigation coordinate is required, there is a disadvantage that the calculation amount is increased.

Strapdown has been proposed and put into practical use since the processing speed of the computer has become able to handle the computational complexity of the system as the computer develops. At present, research on Strapdown is the mainstream, and in this study, Strapdown is applied to the experiment.

2.2.4 INS configuration and error factors

Inertial Measurement Unit (IMU) sensor used in the INS consists of an accelerometer and a gyroscope. Accelerometer is a sensor that can sense the motion of an object by detecting dynamic forces such as acceleration and vibration. A gyroscope is an instrument that detects the angular velocity of an object and is often called a gyro.

In addition, IMU sensors generally have bias error (b) and noise error (w). This can be expressed as (2.18), if it is an accelerometer measurement (f_{meas}) and a gyroscope measurement (ω_{meas}).

$$\begin{aligned} f_{meas} &= f_{true} + b_f + w_f \\ \omega_{meas} &= \omega_{true} + b_\omega + w_\omega \end{aligned} \tag{2.18}$$

Since the error level differs according to the level of the sensor, it can be selected appropriately considering the purpose of use and practicality. Table 1 shows the classification according to sensor performance.

Table 1. IMU sensor classification by performance

	Gyro bias ($\deg/hr$)	**Gyro noise** ($\deg/\sqrt{hr}$)	**Accel. Bias** (μg)	**Accel. Noise** (m/s^2)
Navigation	0.01 ~ 0.1	0.005	50	0.001
Tactical	0.1 ~ 1	0.125	500	0.01
Automotive	1 ~ 30	0.3 ~	30,000 ~	0.05 ~

2.2.5 IMU sensor analysis

IMU sensor used in this paper uses the IMU sensor installed inside the Ublox-M8T GPS receiver. We confirmed that the datasheet provided by Ublox does not provide information on the IMU sensor, so we performed the Allan variance analysis to check the performance of the IMU sensor [30].

In order to perform the Allan variance analysis, the measured static data of the IMU sensor were collected for 12 hours. This allows the noise level of the sensor to be determined.

① Accelerometer Allan variance analysis

Figure 11 shows the Allan variance for the x, y, and z axes of the accelerometer using the collected data.

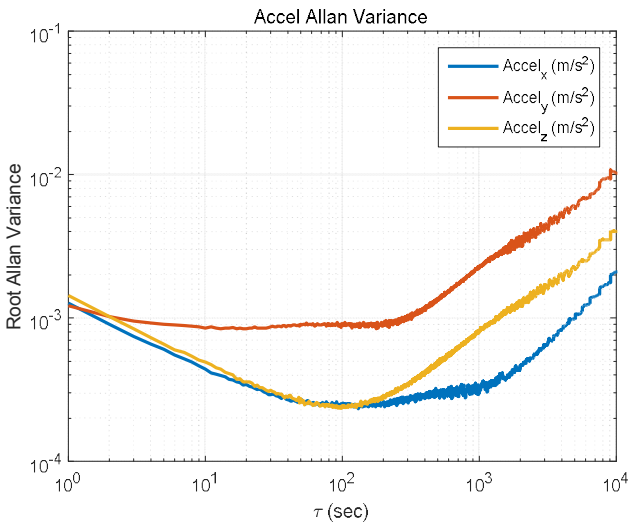

Figure 11. Accelerometer Allan variance.

At this time, the root Allan variance value at $\tau = 10^0 = 1$ becomes the random walk value of the sensor. Therefore, the random walk values for each axis are summarized in Table 2.

Table 2. Accelerometer Velocity Random Walk

Accelerometer Velocity Random Walk(VRW) [$m / s / \sqrt{Hz}$]	
x-axis	0.00127
y-axis	0.00122
z-axis	0.00143

In order to apply the noise level conservatively to the system to be constructed in the system, the value of the z-axis, which is the largest value among the VRW values for each axis, is applied to all the axes.

In the case of bias, the specification of MEMS sensor with similar VRW value is applied and it is 50mg considering only constant random bias error.

② **Gyroscope Allan variance analysis**

Figure 12 shows the Allan variance for the x,y, and z axes of the gyroscope using the collected data.

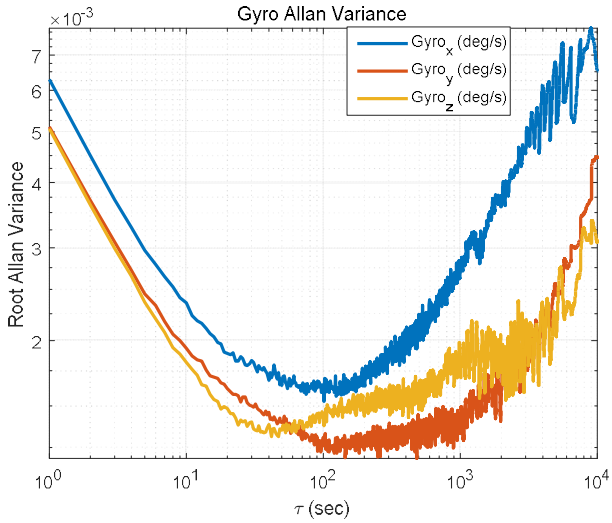

Figure 12. Gyroscope Allan variance

At this time, the root Allan variance value at $\tau = 10^0 = 1$ becomes the random walk value of the sensor. Therefore, the random walk values for each axis are summarized in Table 3.

Table 3. Gyroscope Angular Random Walk

Gyroscope Angular Random Walk(ARW) [$\mathrm{deg}/\sqrt{Hz}$ **]**	
x-axis	0.00629
y-axis	0.00510
z-axis	0.00507

In order to apply the noise level conservatively to the system to be constructed in the system, like accelerometer, the x-axis value, which is the largest value among the ARW values of each axis, is applied to all the axes.

In the case of bias, the specification of MEMS sensor with similar ARW value is applied and it is $3\,\mathrm{deg/sec}$ considering only constant random bias error.

2.3 GPS/INS integration

2.3.1 GPS/INS integrated navigation overview

GPS is the most commonly used system in outdoor navigation because it can obtain position worldwide with low cost receiver and the error is constant regardless of time. However, due to the characteristics of radio navigation, there are disadvantages such as jamming and sensitivity to the external environment and when there is a building blocking radio wave like in the city center, GPS signal disconnection occurs and the navigation error increases.

Since INS is a independent navigation system, it can provide continuous and high navigation without being influenced by the outside. However, since the position and attitude are obtained by integrating, the error accumulates with time, and there is a disadvantage that the navigation solution emits in the end.

By integrating GPS and INS, the advantages and disadvantages of each other can be complemented. As a result, a system can be realized that provides stable navigation and navigation and increases the output rate [31].

Table 4. Compare of GPS and INS

	GPS	INS
How to calculate navigation solution	Radio navigation (Triangulation method)	Guess navigation (Acceleration, angular velocity integral)
Advantage	-Low price -Globally operable -Bounded error -High accuracy	-Independent navigation -High navigation output rate - Continuity
Disadvantage	-Sensitive to external environment -Vulnerable to jamming	-Expensive equipment -Divergence of error over time -A lot of computation

2.3.2 GPS/INS integrated navigation limit

GPS/INS integrated navigation is complementary to each other's strengths and weaknesses to provide a stable navigational solution, as well as navigation and high output, so it is also used for high-frequency vehicle. However, there is a disadvantage that the attitude information can not be calculated if the vehicle is stopped or moves very slowly.

In this paper, we solve the problem by supplementing the disadvantage by adding a magnetometer which can supplement the attitude information.

2.4 Magnetometer

2.4.1 Magnetometer overview

The Earth's magnetic field is measured at the Earth's surface at about 0.25 to 0.65 Gauss. Magnetometer is a device that measures the magnetic field of this earth. The magnetic north of the earth is measured by the magnetic field of the earth and the true north is calculated by correcting it using declination between magnetic north and true north and inclination between horizontal plane and magnetic field vector.

This true north can be used to determine the attitude of the vehicle.

2.4.2 Magnetometer error factor and correction method

There are two major causes of error in the magnetometer. It is a hard iron and soft iron. Hard iron error is an error due to the influence of metals magnetized around the magnetometer. It is characterized by a bias type error. The soft iron error is an error caused by the distortion caused by the interaction with the earth's magnetic field.

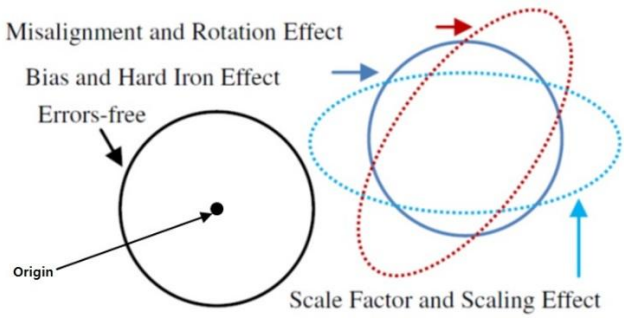

Effect of errors on magnetic field measurement locus (Gebre-Egziabher, 2001).

Figure 13. Magnetometer error factor and calibration process

Also, when the measured magnetometer raw data is plotted on the x and y coordinates, an elliptical magnetic field is drawn, but the center is not the origin. As the calibration progresses, the ellipse becomes a circle whose center is the origin. The procedure for removing the error of the magnetometer is as follows.

① **Hard iron error compensation**

Subtract the bias from the magnetometer raw data. Subtract the bias and the center of the ellipse will come to the origin.

② **Soft iron error compensation**

In the measurement of the elliptical shape, the major axis is rotated so as to be located on the x-axis. Then, scaling the x and y-axis data to fit the actual magnetic field size. When the scaling is completed, rotate the scale backward by the size that was initially rotated. After these two stages of compensation,

the error of the magnetometer is removed and the attitude of the vehicle is calculated using the corrected data.

2.5 GPS/INS/Magnetometer integration

2.5.1 GPS/INS/Magnetometer algorithm overview

In this study, to realize the GPS/INS/Magnetometer integrated navigation system suitable for the land vehicle, 2D is assumed considering the characteristics of the land vehicle [32]. Also, before applying the system to the actual measurement, simulation is implemented and the system is verified to predict the performance. Simulation can be used to predict the performance of actual measurements. Finally, the experiment was conducted in real environment to verify the system.

2.5.2 2D Extended Kalman Filter for land vehicle

2.5.2.1 Simplified INS navigation equation

A commonly used 3D INS navigation equation can consist of latitude (ϕ_T), longitude (λ_T), height (h), velocity expressed by NED coordinate (v_N, v_E, v_D), and attitude expressed by Euler angles (Roll [ϕ], Pitch [θ], Yaw [ψ]). It is same as (2.19),(2.20),(2.21) in the formula.

$$\dot{\phi}_T = \frac{v_N}{(R+h)},\ \dot{\lambda}_T = \frac{v_E}{(R+h)\cos\phi_T},\ \dot{h} = -v_D \quad (2.19)$$

where, R : radius of earth

$$\dot{\mathbf{v}}_e^n = C_b^n \mathbf{f}^b + \mathbf{g}_l^n - \left(2\boldsymbol{\omega}_{ie}^n + \boldsymbol{\omega}_{en}^n\right) \times \mathbf{v}_e^n \quad (2.20)$$

where, $\mathbf{v}_e^n = [v_N \quad v_E \quad v_D]^{\mathrm{T}}$

$\mathbf{f}^b = \begin{bmatrix} f_x & f_y & f_z \end{bmatrix}^T$: *Accel. output*

$\mathbf{g}_l^n$: local gravity

$\boldsymbol{\omega}_{en}^n$: transport rate

$\boldsymbol{\omega}_{ie}^n$: earth rotation rate

$$\begin{bmatrix} \dot{\phi} \\ \dot{\theta} \\ \dot{\psi} \end{bmatrix} = \begin{bmatrix} 1 & \sin\phi\tan\theta & \cos\phi\tan\theta \\ 0 & \cos\phi & -\sin\phi \\ 0 & \sin\phi\sec\theta & \cos\phi\sec\theta \end{bmatrix} \begin{bmatrix} p \\ q \\ r \end{bmatrix} \quad (2.21)$$

where, $\boldsymbol{\omega}_{nb}^b = \begin{bmatrix} p & q & r \end{bmatrix}^T = \boldsymbol{\omega}_{ib}^b - C_n^b\left(\boldsymbol{\omega}_{ie}^n + \boldsymbol{\omega}_{en}^n\right)$

$\boldsymbol{\omega}_{ib}^b = \begin{bmatrix} \omega_x & \omega_y & \omega_z \end{bmatrix}^T$: gyroscope output

These navigation equations can be simplified by using low cost IMU sensors and land vehicle characteristics.

First, it is appropriate to use a low-cost IMU sensor if it emphasizes generalization and practicality. Therefore, in this paper, a low-cost MEMS IMU sensor is used. Using a low-cost IMU sensor, the earth rotation angular

velocity ($\boldsymbol{\omega}_{ie}^{n}$) and the transport rate ($\boldsymbol{\omega}_{en}^{n}$) measured due to the spherical shape of the earth are below the noise level of the sensor, so measurement is impossible and can be ignored ($\boldsymbol{\omega}_{ie}^{n}, \boldsymbol{\omega}_{en}^{n} \approx 0$). Therefore, the term is removed from the 3D INS navigation equations and is the same as (2.22).

$$\begin{aligned} \dot{\mathbf{v}}_{e}^{n} &= C_{b}^{n}\mathbf{f}^{b} + \mathbf{g}_{l}^{n} - \cancel{\left(2\boldsymbol{\omega}_{ie}^{n} + \boldsymbol{\omega}_{en}^{n}\right) \times \mathbf{v}_{e}^{n}} \\ \boldsymbol{\omega}_{nb}^{b} &= \boldsymbol{\omega}_{ib}^{b} - \cancel{C_{n}^{b}\left(\boldsymbol{\omega}_{ie}^{n} + \boldsymbol{\omega}_{en}^{n}\right)} \end{aligned} \tag{2.22}$$

Secondly, 3D INS navigation equation is very computationally expensive to construct the system by applying to the land vehicle, so we consider simplification of the system considering the characteristics of the land vehicle. The assumption is that there is no change in height because the land vehicle attach to the ground. Therefore, it is possible to simplify to 2D, and accordingly it is possible to assume roll and pitch to be zero. Finally, 3D INS navigation equation is reconstructed by 2D INS navigation equations such as (2.23), (2.24) and (2.25).

$$\dot{\phi}_{T} = \frac{V_{N}}{R}, \quad \dot{\lambda}_{T} = \frac{V_{E}}{R\cos\phi_{T}} \tag{2.23}$$

$$\begin{bmatrix} \dot{V}_{N} \\ \dot{V}_{E} \end{bmatrix} = C_{b}^{n}(\psi)\begin{bmatrix} f_{x} \\ f_{y} \end{bmatrix}, \quad C_{b}^{n}(\psi) = \begin{bmatrix} \cos\psi & -\sin\psi \\ \sin\psi & \cos\psi \end{bmatrix} \tag{2.24}$$

$$\dot{\psi} = \omega_{z} \tag{2.25}$$

2.5.2.2 2D Extended Kalman Filter configuration for land vehicle

Extended Kalman Filter is constructed using the simplified 2D INS navigation equation. Extended Kalman Filter is a Kalman Filter used in linear systems applied to nonlinear systems. At this time, the nonlinear system model is linearized using Taylor series. Therefore, 2D INS navigation equations are modeled using Taylor series. For Taylor series expansion for each state, it consists of (2.26),(2.27),(2.28),(2.29),(2.30),(2.31).

$$\begin{aligned}\dot{\hat{\phi}}_T - \delta\dot{\phi}_T &= \frac{V_N}{R}\bigg|_{\hat{\phi}_T} - \frac{\partial}{\partial V_N}\left(\frac{V_N}{R}\right)\delta V_N \\ \Rightarrow \delta\dot{\phi}_T &= \frac{\partial}{\partial V_N}\left(\frac{V_N}{R}\right)\delta V_N \\ &= \frac{\delta V_N}{R}\end{aligned} \tag{2.26}$$

$$\dot{\hat{\lambda}}_T - \delta\dot{\lambda}_T = \frac{V_E}{R\cos\phi_T}\bigg|_{\hat{\lambda}_T} - \frac{\partial}{\partial \phi_T}\left(\frac{V_E}{R\cos\phi_T}\right)\delta\phi_T - \frac{\partial}{\partial V_E}\left(\frac{V_E}{R\cos\phi_T}\right)\delta V_E$$

$$\begin{aligned}\Rightarrow \delta\dot{\lambda}_T &= \frac{\partial}{\partial \phi_T}\left(\frac{V_E}{R\cos\phi_T}\right)\delta\phi_T + \frac{\partial}{\partial V_E}\left(\frac{V_E}{R\cos\phi_T}\right)\delta V_E \\ &= \frac{V_E\tan\phi_T}{R\cos\phi_T}\delta\phi_T + \frac{1}{R\cos\phi_T}\delta V_E\end{aligned} \tag{2.27}$$

$$\dot{\hat{V}}_N - \delta\dot{V}_N = (\cos\psi f_x - \sin\psi f_y)\big|_{\hat{V}_N} - \frac{\partial}{\partial\psi}\left(\cos\psi f_x - \sin\psi f_y\right)\delta\psi$$
$$- \frac{\partial}{\partial b_{ax}}\left(\cos\psi f_x - \sin\psi f_y\right)\delta b_{ax} - \frac{\partial}{\partial b_{ay}}\left(\cos\psi f_x - \sin\psi f_y\right)\delta b_{ay}$$
$$\Rightarrow \delta\dot{V}_N = \frac{\partial}{\partial\psi}\left(\cos\psi f_x - \sin\psi f_y\right)\delta\psi + \frac{\partial}{\partial b_{ax}}\left(\cos\psi f_x - \sin\psi f_y\right)\delta b_{ax} \quad (2.28$$
$$+ \frac{\partial}{\partial b_{ay}}\left(\cos\psi f_x - \sin\psi f_y\right)\delta b_{ay}$$
$$= -(\sin\psi f_x + \cos\psi f_y)\delta\psi - \cos\psi(\delta b_{ax} + w_{ax}) + \sin\psi(\delta b_{ay} + w_{ay})$$
$$= -f_E\delta\psi - \cos\psi(\delta b_{ax} + w_{ax}) + \sin\psi(\delta b_{ay} + w_{ay})$$

$$\dot{\hat{V}}_E - \delta\dot{V}_E = (\sin\psi f_x + \cos\psi f_y)\big|_{\hat{V}_E} - \frac{\partial}{\partial\psi}\left(\sin\psi f_x + \cos\psi f_y\right)\delta\psi$$
$$- \frac{\partial}{\partial b_{ax}}\left(\sin\psi f_x + \cos\psi f_y\right)\delta b_{ax} - \frac{\partial}{\partial b_{ay}}\left(\sin\psi f_x + \cos\psi f_y\right)\delta b_{ay}$$
$$\Rightarrow \delta\dot{V}_E = \frac{\partial}{\partial\psi}\left(\sin\psi f_x + \cos\psi f_y\right)\delta\psi + \frac{\partial}{\partial b_{ax}}\left(\sin\psi f_x + \cos\psi f_y\right)\delta b_{ax} \quad (2.29$$
$$+ \frac{\partial}{\partial b_{ay}}\left(\sin\psi f_x + \cos\psi f_y\right)\delta b_{ay}$$
$$= (\cos\psi f_x - \sin\psi f_y)\delta\psi - \sin\psi(\delta b_{ax} + w_{ax}) - \cos\psi(\delta b_{ay} + w_{ay})$$
$$= f_E\delta\psi - \sin\psi(\delta b_{ax} + w_{ax}) - \cos\psi(\delta b_{ay} + w_{ay})$$

$$\dot{\hat{\psi}} - \delta\dot{\psi} = \omega_z\big|_{\hat{\psi}} - \frac{\partial}{\partial b_{gz}}(\omega_z)\delta b_{gz}$$
$$\Rightarrow \delta\dot{\psi} = -\delta b_{gz} - w_{gz} \quad (2.30)$$

Bias has a constant value. Therefore, it can be expressed as (2.31).

$$\delta\dot{b}_{ax} = \delta\dot{b}_{ay} = \delta\dot{b}_{gz} = 0 \tag{2.31}$$

State is 8 in total, including position (latitude, longitude), velocity (east, north), accelerometer x, y axis bias, and gyroscope z axis bias. Using this, state equation is like matrix (2.32).

$$\begin{bmatrix} \delta\dot{\phi}_T \\ \delta\dot{\lambda}_T \\ \delta\dot{V}_N \\ \delta\dot{V}_E \\ \delta\dot{\psi} \\ \delta\dot{b}_{a.x} \\ \delta\dot{b}_{a.y} \\ \delta\dot{b}_{g.z} \end{bmatrix} = \begin{bmatrix} 0 & 0 & \frac{1}{R} & 0 & 0 & 0 & 0 & 0 \\ \frac{v_E}{R}\frac{\tan\phi_T}{\cos\phi_T} & 0 & 0 & \frac{1}{R\cos\phi_T} & 0 & 0 & 0 & 0 \\ 0 & 0 & 0 & 0 & -f_E & -\cos\psi & \sin\psi & 0 \\ 0 & 0 & 0 & 0 & f_N & -\sin\psi & -\cos\psi & 0 \\ 0 & 0 & 0 & 0 & 0 & 0 & 0 & -1 \\ 0 & 0 & 0 & 0 & 0 & 0 & 0 & 0 \\ 0 & 0 & 0 & 0 & 0 & 0 & 0 & 0 \\ 0 & 0 & 0 & 0 & 0 & 0 & 0 & 0 \end{bmatrix} \begin{bmatrix} \delta\phi_T \\ \delta\lambda_T \\ \delta V_N \\ \delta V_E \\ \delta\psi \\ \delta b_{a.x} \\ \delta b_{a.y} \\ \delta b_{g.z} \end{bmatrix}$$

$$+ \begin{bmatrix} 0 & 0 & 0 \\ 0 & 0 & 0 \\ -\cos\psi & \sin\psi & 0 \\ -\sin\psi & -\cos\psi & 0 \\ 0 & 0 & -1 \\ 0 & 0 & 0 \\ 0 & 0 & 0 \\ 0 & 0 & 0 \end{bmatrix} \begin{bmatrix} w_{ax} \\ w_{ay} \\ w_{gz} \end{bmatrix} \tag{2.32}$$

In addition, measurement update in the measurement equation is updated every 1 second because the GPS measurement is updated to 1 Hz and the magnetometer measurement is updated to 10 Hz as shown in Figure 14, and only the magnetometer is updated every 0.1 second.

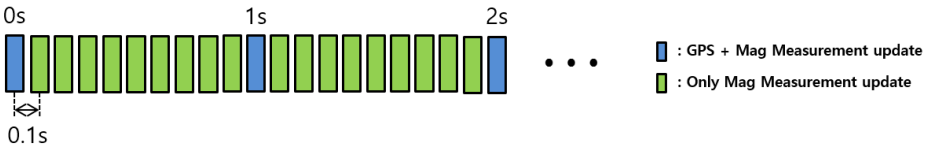

Figure 14. Measurement update sequence.

GPS measurement updates position, velocity, and heading as in (2.33).

$$z_{GPS} = \begin{bmatrix} \phi_{T,GPS} & \lambda_{T,GPS} & v_{N,GPS} & v_{E,GPS} & \psi_{GPS} \end{bmatrix}^T = \mathrm{H}_{GPS} x + V_{GPS} \tag{2.33}$$

$$where,\ H_{GPS} = \begin{bmatrix} I_{5\times5} & 0_{5\times3} \end{bmatrix}$$

$$V_{GPS} = diag\left[\left(\sigma_{\phi_T,GPS}\right)^2,\ \left(\sigma_{\lambda_T,GPS}\right)^2,\ \left(\sigma_{\mathrm{V}_N,GPS}\right)^2,\ \left(\sigma_{\mathrm{V}_E,GPS}\right)^2,\ \left(\sigma_{\delta\psi}\right)^2 \right]$$

Position and velocity obtained from the GPS receiver, and heading is obtained by using GPS velocity measurement (2.34).

$$\psi_{GPS} = \tan^{-1}\left(\frac{V_{E,GPS}}{V_{N,GPS}}\right) \tag{2.34}$$

Magnetometer measurement updates only the heading as in (2.35).

$$z_{Mag} = \begin{bmatrix} \psi_{Mag} \end{bmatrix} = \mathrm{H}_{Mag} x + v_{Mag} \tag{2.35}$$

$$where,\ \ H_{Mag} = \begin{bmatrix} 0\,0\,0\,0\,1\,0\,0\,0 \end{bmatrix}$$

$$V_{Mag} = (\sigma_{Mag})^2$$

Heading can be obtained from the x and y axis measurements of the magnetometer (2.36) and can be easily confirmed by the diagram in Figure 15. Also, when calculating the magnetometer heading, the angle of declination should always be corrected.

$$\psi_{Mag} = -\tan^{-1}\left(\frac{B_{\text{y.Mag}}}{B_{\text{x.Mag}}}\right) + \delta(\text{declination}) \tag{2.36}$$

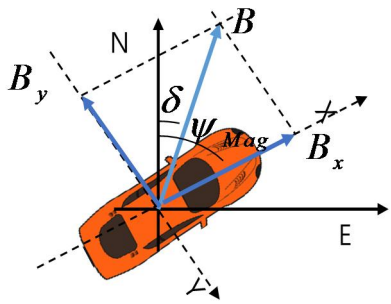

Figure 15. Magnetometer Heading

3. Simulation

2D Extended Kalman Filter considering the characteristics of the land vehicle is constructed in the previous chapter. Simulation is performed to check the performance of the configured filter and to determine whether there is a defect.

3.1 Simulation data generation

In order to simulation, we create true position, velocity, and attitude based on configured scenario. Measured value of the IMU sensor and the magnetometer is generated using the true value.

① Simulation true position, velocity, heading data generation

Simulation true position, velocity, and heading data is generated in the following order.

i) After assuming a plane, select the desired scenario. (NED acceleration setting)

ii) NED velocity is calculated by integrating the NED acceleration constituted in i) (2D, downward velocity zero)

iii) Based on NED velocity, heading is calculated by (3.1).

$$\psi = \tan^{-1}\left(\frac{V_E}{V_D}\right) \tag{3.1}$$

iv) After setting the initial position and position is created using NED velocity and attitude obtained previously. (Δt is very small, ignore numerical error)

$$\begin{aligned} \phi_T(k+1) &= \dot{\phi}_T(k)\Delta t + \phi_T(k) \\ \lambda_T(k+1) &= \dot{\lambda}_T(k)\Delta t + \lambda_T(k) \\ h &= 0 \end{aligned} \tag{3.2}$$

$$where, \quad \dot{\phi}_T = \frac{v_N}{R}, \quad \dot{\lambda}_T = \frac{v_E}{R\cos\phi_T}, \quad \dot{h} = 0$$

② **Simulation GPS data generation**

GPS data is generated considering the general error level of DGPS in the true position and velocity data, and error is generated by applying the error of 1m at the position and 0.1m/s at the velocity based on 1σ. Heading is obtained by using the velocity of GPS, so it has different error level according to the velocity of GPS.

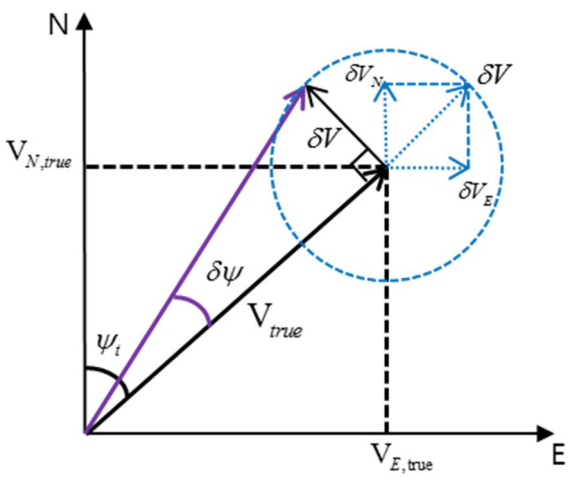

Figure 16. GPS Heading error configuration

Assuming that the error level of each axis of the GPS velocity is equal to σ_V as shown in Figure 16, the error component perpendicular velocity (δV) to the actual velocity (V_{true}) is the error level $\sqrt{2}\sigma_V$. Therefore, the heading error ($\delta\psi$) has a relationship of $\delta\psi \cong \tan\delta\psi = \frac{\delta V}{|V_{true}|}$.

As a result, it can be modeled as having an error level of $\sigma_{\delta\psi} = \frac{\sqrt{2}\sigma_V}{|V_{true}|}(rad)$.

Heading error level modeling applied to the simulation using the modeling equation is shown in Figure 17. Basically, GPS heading error level is inversely proportional to the land vehicle speed, but GPS heading is judged to be reliable only when the $3\sigma_{\delta\psi}$ value is within 5deg.

As a result, GPS heading should be used when the speed is more than 12.4 km / h.

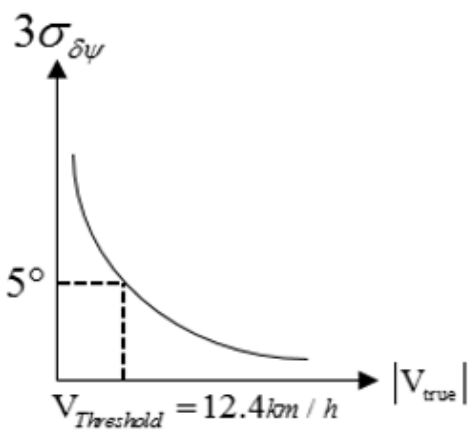

Figure 17. GPS Heading error modeling

③ Simulation IMU sensor data generation

Body frame accelerometer and gyroscope data are generated using the calculated true position, velocity, and heading data.

i) Accelerometer data generation

$$\mathbf{f}^b = C_n^b \left(\dot{\mathbf{v}}_e^n - \mathbf{g}_l^n - \mathbf{v}_e^n \times \boldsymbol{\omega}_{en}^n \right) \tag{3.3}$$

$$where,\ \boldsymbol{\omega}_{en}^n = \begin{bmatrix} \frac{v_E}{R} & -\frac{v_N}{R} & -\frac{v_E \tan\phi_T}{R} \end{bmatrix}^T$$

When the measured data of the accelerometer is generated using the generated true acceleration data, it is configured as (3.4).

$$f_{IMU}(t) = \begin{bmatrix} f_{IMU,x}(t) \\ f_{IMU,y}(t) \end{bmatrix} = a_{true}(t) + b_f + w_f(t) \tag{3.4}$$

$$where,\ b_f = \begin{bmatrix} b_{a,x} \\ b_{a,y} \end{bmatrix},\ w_f(t) = \begin{bmatrix} w_{a,x}(t) \\ b_{a,y}(t) \end{bmatrix}$$

ii) Gyroscope data generation

$$\begin{bmatrix} p \\ q \\ r \end{bmatrix} = \begin{bmatrix} 1 & 0 & -\sin\theta \\ 0 & \cos\phi & \sin\phi\cos\theta \\ 0 & -\sin\phi & \cos\phi\cos\theta \end{bmatrix} \begin{bmatrix} \dot{\phi} \\ \dot{\theta} \\ \dot{\psi} \end{bmatrix} \tag{3.5}$$

$$\boldsymbol{\omega}_{ib}^b = \boldsymbol{\omega}_{nb}^b + C_n^b \boldsymbol{\omega}_{en}^n$$

$$
\begin{aligned}
&where,\ \ \boldsymbol{\omega}_{ib}^{b} = [\omega_x, \omega_y, \omega_z]^T : gyro\ output \\
&\qquad \boldsymbol{\omega}_{en}^{n} = [\dot{\lambda}_T \cos\phi,\ -\dot{\phi},\ \dot{\lambda}_T \sin\phi]^T : Transport\ rate \\
&\qquad \boldsymbol{\omega}_{nb}^{b} = [p \quad q \quad r]^T
\end{aligned}
$$

When the measured data of the gyroscope is generated using the generated true angular velocity data, it is configured as (3.6).

$$\omega_{IMU}(t) = \omega_{IMU,z}(t) = \omega_{true,z}(t) + b_{g,z} + w_{g,z}(t) \tag{3.6}$$

④ Simulation magnetometer data generation

True data of the magnetometer is provided by National Oceanic and Atmosphere Administration (NOAA). Declination correction is also used by NOAA. In addition, due to the characteristics of the magnetometer, actual data require hard and soft iron for bias correction due to metal objects or magnetic materials around. However, assuming that all calibration is completed, simulation data is generated by adding only noise to true data as in (3.7).

$$m_{mag}(t) = \begin{bmatrix} m_{mag,x}(t) \\ m_{mag,y}(t) \end{bmatrix} = C_n^b(t) \cdot m_{true}^n + w_{mag}(t) \qquad (3.7)$$

$$where,\ \ m_{true}^n = \begin{bmatrix} m_{true,N}^n \\ m_{true,E}^n \end{bmatrix},\ \ w_{mag}(t) = \begin{bmatrix} w_{mag,N}(t) \\ w_{mag,E}(t) \end{bmatrix},\ \ w_{mag}(t) \sim N(0,\ (0.005gauss)^2)$$

3.2 2D Extended Kalman Filter algorithm for land vehicle verification

3.2.1 Simulation scenario

The scenario configuration is configured as shown in Figure 18 to include stop, straight, and turn section, and the total simulation time is 115 seconds.

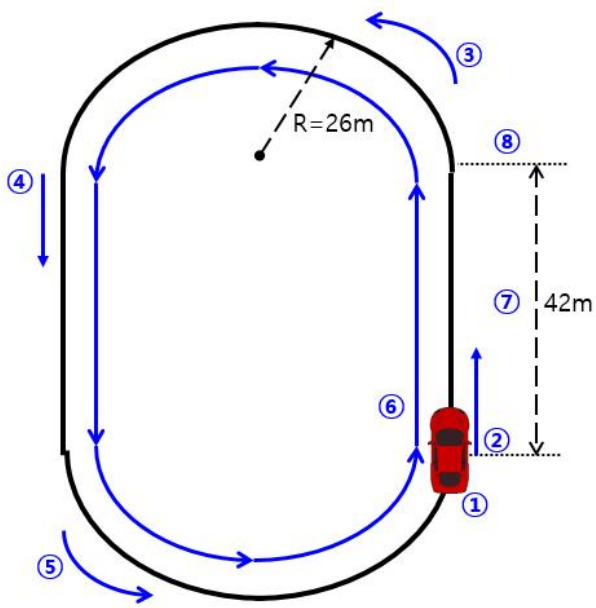

Figure 18. Simulation scenario configuration

① Stop section (5 sec)

② Straight acceleration section (10 sec): Constant acceleration from 0 to 30km/h.

③ Constant velocity turning section (10 sec)

④ Constant velocity straight-line section (5 sec): Constant speed of 30km/h.

⑤ Constant velocity turning section (10 sec)

⑥ 2 tracks of constant velocity (60 sec)

⑦ Deceleration straight-line section (10 sec): Constant Deceleration from 30 to 0km/h

⑧ Stop section (5 sec)

3.2.2 Simulation result

For the analysis of the results, DGPS only, DGPS/INS and DGPS/INS/Magnetometer are compared and analyzed.

3.2.1.1 East, North position error compare

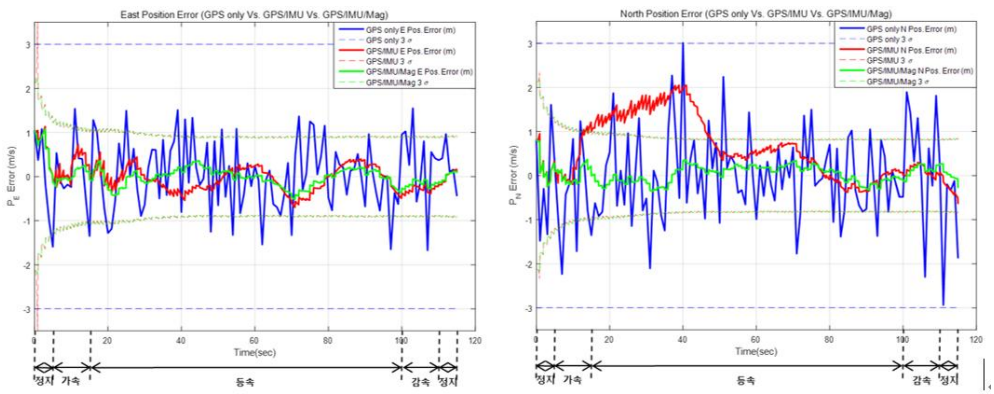

Figure 19. Simulation East, North position error plot.

Table 5. Simulation East position error result.

	DGPS only	DGPS/INS	DGPS/INS/Mag
East position error rms	0.7786m	0.3236m	0.2426m
Improve position accuracy	-	58.4%	68.8%

Table 6. Simulation North position error result.

	DGPS only	DGPS/INS	DGPS/INS/Mag
North position error rms	1.0295m	0.8996m	0.1936m
Improve position accuracy	-	12.6%	81.2%

As for the position error of each axis, it is confirmed that the position accuracy improvement is 58.4% for East and 12.6% for North when INS is added compared with DGPS only. In addition, when magnetometer is additionally used, it can be seen that the improvement of position accuracy is better at 68.8% in East and 81.2% in North.

3.2.1.2 Horizontal position error compare

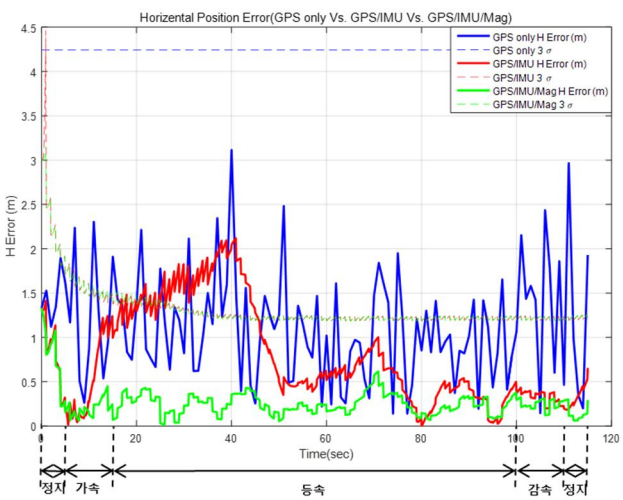

Figure 20. Simulation horizontal position error plot.

Table 7. Simulation horizontal position error result.

	DGPS only	DGPS/INS	DGPS/INS/Mag
Horizontal position error rms	1.2908m	0.9560m	0.3103m
Improve position accuracy	-	25.9%	75.9%

In the horizontal position error, DGPS/INS cannot know heading information in the initial stop section, so that it can be confirmed that the horizontal position error increases sharply in the initial acceleration section. It is confirmed that the horizontal position accuracy is improved by 25.9% compared with DGPS only.

In case of using additional magnetometer, heading information can be always provided in all sections including the stop section, so that the initial heading problem occurred in DGPS / INS is solved and it is confirmed that the horizontal position accuracy is improved by 75.9% compared to DGPS only.

3.2.1.3 Heading error compare

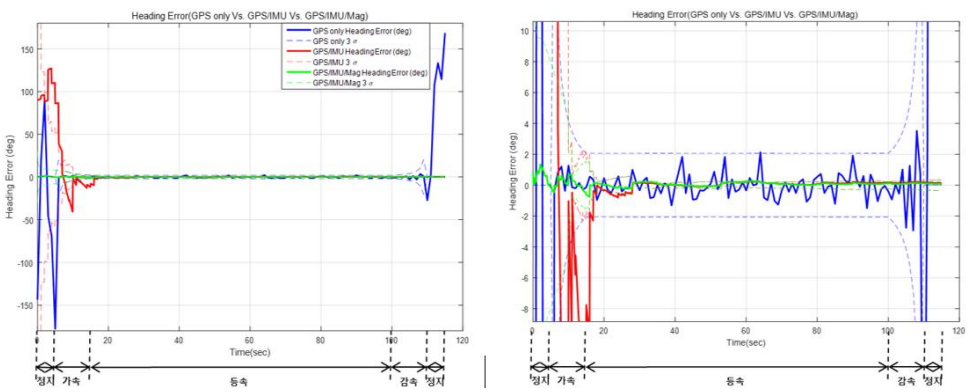

Figure 21. Simulation heading error plot.

DGPS only cannot obtain information about heading when the vehicle is stopping or driving at low speed. Therefore, it can be confirmed that the heading error is very large, and GPS/INS is also estimated by using gyroscope, but heading diverges over time. However, in case of DGPS/INS/Magnetometer

equipped with additional magnetometer, stable heading information can be obtained at all sections.

3.2.1.4 Bias error compare

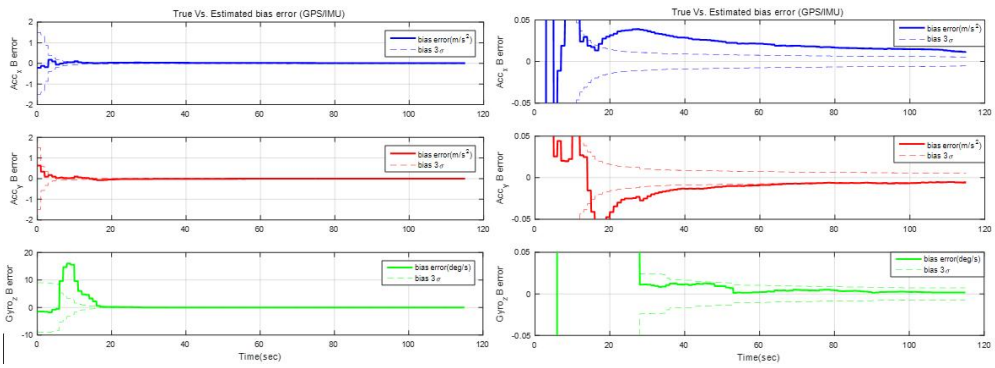

Figure 22. Simulation DGPS/INS bias error plot.

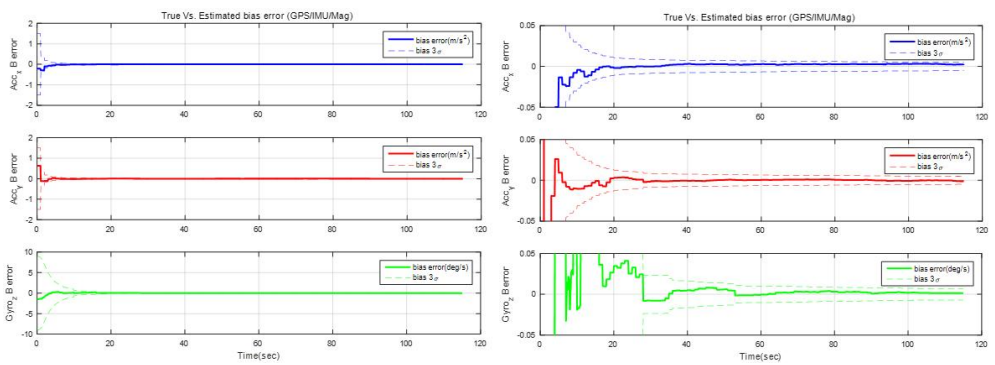

Figure 23. Simulation DGPS/INS/Magnetometer bias error plot.

The results of the bias estimation for DGPS/INS are shown in Figure 22, and the results for DGPS/INS/Magnetometer are shown in Figure 23. Accelerometer x, y axis bias estimation results and Gyroscope z axis bias

estimation results are shown in the order of the graphs, and the enlarged graph is shown on the right.

As a result, in the case of DGPS/INS, it is confirmed that does not fall within the 3σ of the accelerometer x, the y-axis bias and the gyroscope z-axis bias occurs. However, in the case of DGPS/INS/Magnetometer equipped with a magnetometer, it can be confirmed that the bias can be estimated by entering 3σ in all the sections.

4. Actual experiment

Simulation has confirmed the performance defects of the 2D DGPS/INS/Magnetometer combined system for land vehicle and confirmed the performance improvement. In this section, verifying the performance of the actual data after applying it to the actual experiment using the simulation proven system.

4.1 System configuration

4.1.1 Considerations when processing actual data

In the actual data processing, there is a problem to be considered in addition to the simulation data processing. In the process of simplifying the 3D INS navigation equation into the 2D INS navigation equation, the assumption that the roll and pitch are 0 is applied. When the land vehicle is driving, pitch is generated in the acceleration and deceleration, and roll occurs in the turning section. This has a not negligible impact.

Therefore, in this paper, we have summarized the following considerations in order to reflect these effects on the system.

4.1.1.1 Accelerometer considerations

Since the existing accelerometer measurement model has Roll and Pitch of 0, gravity components are not measured on the x and y axes of the accelerometer. Therefore, it is reasonable to consider constant bias. Finally, accelerometer x, y axis measurement model consists of true data, constant bias, and noise. The equation is expressed as (4.1) on the x-axis and (4.2) on the y-axis.

$$x-axis:\ f_{ax,meas}(\mathrm{t}) = f_{ax,true}(t) + b_{ax} + w_{ax}(\mathrm{t}) = a_x(\mathrm{t}) + b_{ax} + w_{ax}(\mathrm{t}) \quad (4.1)$$

$$where,\ f_{ax,true}(t) = a_x(\mathrm{t})$$

$$y-axis:\ f_{ay,meas}(\mathrm{t}) = f_{ay,true}(t) + b_{ay} + w_{ay}(\mathrm{t}) = a_y(\mathrm{t}) + b_{ay} + w_{ay}(\mathrm{t}) \quad (4.2)$$

$$where,\ f_{ay,true}(t) = a_y(\mathrm{t})$$

However, in the case of actual measured data, as shown in Figure 24, when a land vehicle turns, accelerates, or decelerates, rolls and pitches are generated. As a result, gravity components are measured in the actual accelerometer measurement data.

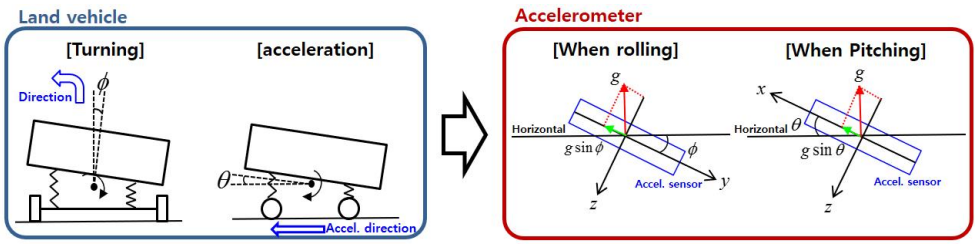

Figure 24. Effect of accelerometer on vehicle behavior.

Therefore, accelerometer measurement data should use model with gravity component. The models considering gravity components are represented by the accelerometer x axis (4.3) and the y axis (4.4).

$$
\begin{aligned}
x-axis: \quad f_{ax,meas}(t) &= f_{ax,true}(t) + b_{ax.0} + w_{ax}(t) \\
&= a_x(t) + (g \cdot \sin\theta(t) + b_{ax.0}) + w_{ax}(t) \\
&= a_x(t) + (b_{ax.1}(t) + b_{ax.0}) + w_{ax}(t) \;=\; a_x(t) + b_{ax}(t) + w_{ax}(t)
\end{aligned} \tag{4.3}
$$

$$
where, \quad f_{ax,true}(t) = a_x(t) + g \cdot \sin\theta(t)
$$

$$
b_{ax}(\mathrm{t}) \square\; b_{ax.1}(\mathrm{t}) + b_{ax.0}
$$

$$
\begin{aligned}
y-axis: \quad f_{ay,meas}(\mathrm{t}) &= f_{ay,\mathrm{true}}(\mathrm{t}) + b_{ay}(\mathrm{t}) + w_{ay}(\mathrm{t}) \\
&= a_y(\mathrm{t}) + (-g \cdot \sin\phi(\mathrm{t}) + b_{ay.0}) + w_{ay}(\mathrm{t}) \\
&= a_y(\mathrm{t}) + (b_{ay.1}(\mathrm{t}) + b_{ay.0}) + w_{ay}(\mathrm{t}) \;=\; a_y(\mathrm{t}) + b_{ay}(\mathrm{t}) + w_{ay}(\mathrm{t})
\end{aligned} \tag{4.4}
$$

$$
where, \quad f_{ay,true}(t) = a_y(t) - g \cdot \sin\phi(t)
$$

$$
b_{ay}(\mathrm{t}) \square\; b_{ay.1}(\mathrm{t}) + b_{ay.0}
$$

In order to apply this new model to the system, the time varying bias is applied considering the part where the constant bias is applied and the gravitational term, which was modeled by the random walk and reflected in the system.

As a result, accelerometer x-axis bias model is defined in (4.3) and the size of $\dot{b}$ can be mathematically confirmed by using (4.5).

$$
\begin{aligned}
\dot{b}_{ax}(\mathrm{t}) = \dot{b}_{ax.1}(\mathrm{t}) &= g\cos\theta(\mathrm{t})\,\dot{\theta}(\mathrm{t}) \\
&\cong g\dot{\theta}(\mathrm{t}) \quad (\because |\theta(\mathrm{t})| \le 3^\circ \;\rightarrow \cos\theta(\mathrm{t}) \approx 1)
\end{aligned} \tag{4.5}
$$

The y-axis bias model of the accelerometer is also defined in (4.4), and the size of $\dot{b}$ can be mathematically confirmed as in (4.6).

$$\dot{b}_{ay}(\mathrm{t}) = \dot{b}_{ay.1}(\mathrm{t}) = -g\cos\phi(\mathrm{t})\dot{\phi}(\mathrm{t})$$
$$\cong -g\dot{\phi}(\mathrm{t}) \quad (\because |\phi(\mathrm{t})| \leq 2^\circ \rightarrow \cos\phi(\mathrm{t}) \approx 1) \tag{4.6}$$

As a result, we confirmed that the $\dot{b}$ term of the accelerometer is a function of $\dot{\theta}(\mathrm{t})$ and $\dot{\phi}(\mathrm{t})$. Therefore, $\dot{\theta}(\mathrm{t})$ and $\dot{\phi}(\mathrm{t})$ values of actual data are analyzed and applied to actual system.

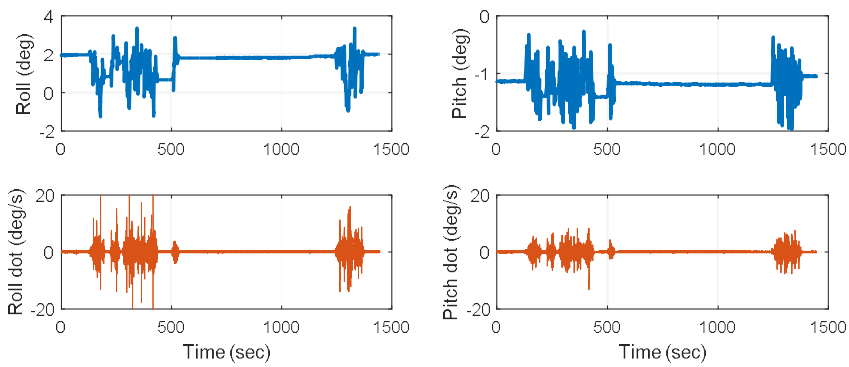

Figure 25. Actual vehicle Roll, Pitch and dot values.

The results are shown in Figure 25. In this case, except for the section where the vehicle is stopped, only the sections where the vehicle is actually driving are analyzed and $\dot{\theta}(\mathrm{t})$ and $\dot{\phi}(\mathrm{t})$ are applied. The result is confirmed to have a value of (4.7) and applied to the system.

$$\dot{\phi}(\mathrm{t}) \sim \mathrm{N}(0, (1.7434^\circ)^2), \quad \dot{\theta}(\mathrm{t}) \sim \mathrm{N}(0, (1.1842^\circ)^2) \tag{4.7}$$

4.1.1.2 Gyroscope considerations

Gyroscope also defined a measurement model under the assumption that roll and pitch are zero. Finally, gyroscope z-axis measurement model consists of true data, constant bias, and noise. This is expressed by the formula (4.8).

$$\omega_{z,meas}(\mathrm{t}) = \omega_{z,true}(t) + b_{gz} + w_{gz}(\mathrm{t}) \tag{4.8}$$

In this case, constant bias is obtained by using the formulas (2.25) and (4.8) for the heading in the 2D INS navigation equation, and the procedure of (4.9) is performed (4.10).

$$\dot{\psi} = \omega_{z,true}(\mathrm{t}) = \omega_{z,\mathrm{meas}}(\mathrm{t}) - b_{gz} - w_{gz}(\mathrm{t}) \ \ (ignore\ of\ Noise) \tag{4.9}$$

$$b_{gz} = \omega_{z,meas} - \dot{\psi} \tag{4.10}$$

However, since the actual gyroscope data is not 0 in Roll and Pitch, it is necessary to consider the axis change of the gyroscope. Finally, gyroscope z-axis measurement model consists of true data, time varying bias, and noise. This can be expressed as (4.11).

$$\omega_{z,meas}(\mathrm{t}) = \omega_{z,true}(t) + b_{gz}(\mathrm{t}) + w_{gz}(\mathrm{t}) \tag{4.11}$$

$$where,\ \ b_{gz}(\mathrm{t}) \square\ b_{\mathrm{gz}.1}(\mathrm{t}) + b_{\mathrm{gz}.0}$$

In this case, the equation relating to the heading among the 3D INS navigation equations is (2.21). Then, applying (2.21) and (4.11) to find time varying bias is (4.12).

$$
\begin{aligned}
b_{gz}(\mathrm{t}) &= \omega_{z,meas}(\mathrm{t}) - \dot{\psi} \\
&= \omega_{z,true}(t) + b_{gz,0} + w_{gz}(\mathrm{t}) - [\sin\phi \cdot \sec\theta \cdot \omega_{y,true}(\mathrm{t}) + \cos\phi \cdot \sec\theta \cdot \omega_{z,true}(\mathrm{t})] \\
&= [1 - \cos\phi \sec\theta] \cdot \omega_{z,true}(t) + b_{gz,0} - \sin\phi \cdot \sec\theta \cdot \omega_{y,true}(\mathrm{t}) \\
&\cong b_{gz,0} - \sin\phi \cdot \omega_{y,true} \\
&= b_{gz,0} + b_{gz,1}(t) \qquad (b_{gz,1}(t) \square -\sin\phi \cdot \omega_{y,true})
\end{aligned}
\tag{4.12}
$$

This new model is modeled as a random walk and reflected in the system. As a result, the $\dot{b}$ term of the gyroscope z-axis bias model can be confirmed as in (4.13).

$$
\begin{aligned}
\dot{b}_{gz}(\mathrm{t}) = \dot{b}_{gz,1}(\mathrm{t}) &= -\cos\phi \cdot \dot{\phi} \cdot \omega_y - \sin\phi \cdot \dot{\omega}_y \\
&\cong -\dot{\phi}(t) \cdot \dot{\theta}(t)
\end{aligned}
\tag{4.13}
$$

As a result, we confirmed that the $\dot{b}$ term of the gyroscope is a function of $\dot{\theta}(\mathrm{t})$ and $\dot{\phi}(\mathrm{t})$. Therefore, we applied the system to the actual system using the previously analyzed $\dot{\theta}(\mathrm{t})$ and $\dot{\phi}(\mathrm{t})$ values (4.7).

4.1.2 Extended Kalman Filter reflecting actual data characteristics

4.1.2.1 Apply modified measurement model

Since simulation considered constant bias, bias process noise is not applied. However, since actual data should consider the time varying bias, bias process

noise is additionally considered, and the state equation of Extended Kalman Filter is constructed as in (4.14).

$$\begin{bmatrix} \delta\dot{\phi}_T \\ \delta\dot{\lambda}_T \\ \delta\dot{V}_N \\ \delta\dot{V}_E \\ \delta\dot{\psi} \\ \delta\dot{b}_{a.x} \\ \delta\dot{b}_{a.y} \\ \delta\dot{b}_{g.z} \end{bmatrix} = \begin{bmatrix} 0 & 0 & \frac{1}{R} & 0 & 0 & 0 & 0 & 0 \\ \frac{v_E}{R}\frac{\tan\phi_T}{\cos\phi_T} & 0 & 0 & \frac{1}{R\cos\phi_T} & 0 & 0 & 0 & 0 \\ 0 & 0 & 0 & 0 & -f_E & -\cos\psi & \sin\psi & 0 \\ 0 & 0 & 0 & 0 & f_N & -\sin\psi & -\cos\psi & 0 \\ 0 & 0 & 0 & 0 & 0 & 0 & 0 & -1 \\ 0 & 0 & 0 & 0 & 0 & 0 & 0 & 0 \\ 0 & 0 & 0 & 0 & 0 & 0 & 0 & 0 \\ 0 & 0 & 0 & 0 & 0 & 0 & 0 & 0 \end{bmatrix} \begin{bmatrix} \delta\phi_T \\ \delta\lambda_T \\ \delta V_N \\ \delta V_E \\ \delta\psi \\ \delta b_{a.x} \\ \delta b_{a.y} \\ \delta b_{g.z} \end{bmatrix}$$

$$+ \begin{bmatrix} 0 & 0 & 0 & 0 & 0 & 0 \\ 0 & 0 & 0 & 0 & 0 & 0 \\ -\cos\psi & \sin\psi & 0 & 0 & 0 & 0 \\ -\sin\psi & -\cos\psi & 0 & 0 & 0 & 0 \\ 0 & 0 & -1 & 0 & 0 & 0 \\ 0 & 0 & 0 & 1 & 0 & 0 \\ 0 & 0 & 0 & 0 & 1 & 0 \\ 0 & 0 & 0 & 0 & 0 & 1 \end{bmatrix} \begin{bmatrix} w_{ax} \\ w_{ay} \\ w_{gz} \\ w_{B,ax} \\ w_{B,ay} \\ w_{B,gz} \end{bmatrix} \tag{4.14}$$

Also, the process noise is configured as (4.15).

$$Q = E\left[ww^T\right] = \begin{bmatrix} \sigma_{ax}{}^2 & 0 & 0 & 0 & 0 & 0 \\ 0 & \sigma_{ay}{}^2 & 0 & 0 & 0 & 0 \\ 0 & 0 & \sigma_{gz}{}^2 & 0 & 0 & 0 \\ 0 & 0 & 0 & \sigma_{B.ax}{}^2 & 0 & 0 \\ 0 & 0 & 0 & 0 & \sigma_{B.ay}{}^2 & 0 \\ 0 & 0 & 0 & 0 & 0 & \sigma_{B.gz}{}^2 \end{bmatrix} \tag{4.15}$$

4.1.2.2 Consider actual DGPS data characteristic

In the simulation, if the error level of the general DGPS is applied, the error level is analyzed and applied based on the actual data in the actual data experiment.

① DGPS position error analysis

Table 8 summarizes the horizontal error rms level by analyzing the actual DGPS position error provided by the GPS receiver.

Table 8. Actual DGPS data based horizontal position error.

DGPS horizontal position error rms	0.951m

Therefore, assuming that the horizontal position error rms is about 1 m and that the error levels in the east and north directions are the same ($\sigma_{P_H} = \sqrt{\sigma_{P_N}{}^2 + \sigma_{P_E}{}^2} = \sqrt{2}\sigma \ \ (if\ \sigma_{P_N} = \sigma_{P_E} = \sigma)$), the error in each axis direction can be considered as $(1\,\mathrm{m}) / \sqrt{2} \cong 0.7\,\mathrm{m}$ level.

② DGPS velocity error analysis

Table 9 summarizes the results of the actual DGPS velocity error provided by the GPS receiver.

Table 9. Actual DGPS data based velocity error.

DGPS East velocity error rms	0.015 m/s
DGPS North velocity error rms	0.020 m/s

Based on the experimental results, we applied 0.020 m/s, which is larger in both axes, to all axes in order to construct the system conservatively.

③ **DGPS Heading error analysis**

In the analysis of the existing simulation data, DGPS heading was set to be used only when $3\sigma_{\delta\psi}$ is within 5deg. However, if the error level is set to a larger value than not using the low accuracy information, heading error modeling is modified as shown in Figure 26 by determining that it can contribute to improving the heading accuracy.

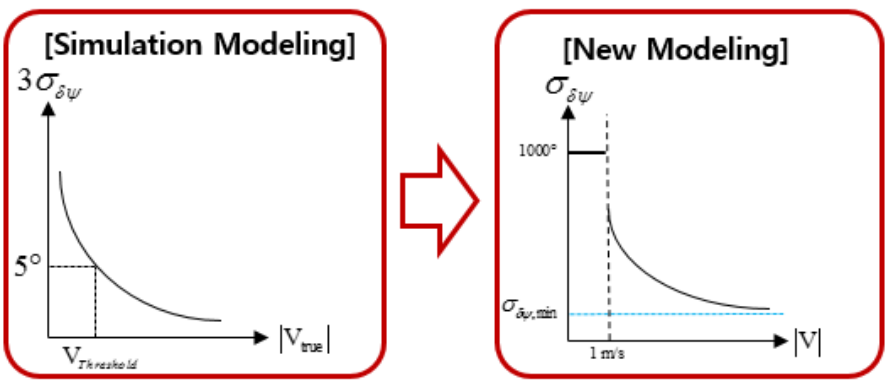

Figure 26. Modify DGPS Heading error model.

As shown in Figure 26, corrected DGPS heading error model is set to 1000deg, which is land vehicle stopped, when heading obtained at DGPS speed is judged to be stopped when the speed is less than 1m/s. Also, in the section where the vehicle is running, the minimum value is set so that the error level does not decrease below 0.5 deg. The reason why 0.5deg is calculated is that the heading error does not go down below 0.5deg in all sections.

4.1.2.3 Consider actual magnetometer data characteristic

It is necessary to calibrate the magnetometer before installing it in the actual land vehicle for the first time. Section 2.4.2 provides a detailed description of the calibration method and allows calibration using the measured data. To make corrections, magnetometer measurement information for all directions of 360 degrees to the vehicle is required, so it drivings 3 or 4 times in the circular motion. Correction is performed using this data as shown in Figure 27.

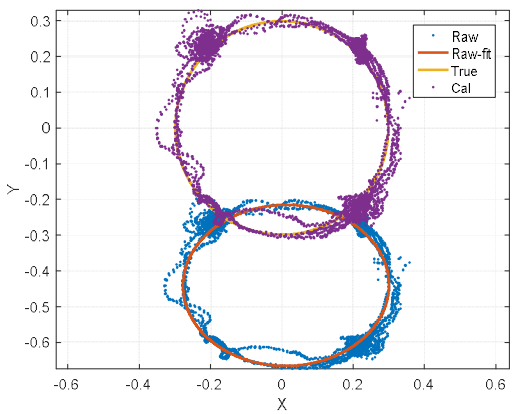

Figure 27. Magnetometer calibration process.

First, when the raw data of the magnetometer is plotted on the x and y axes in units of gauss, a circular shape composed of blue dots is formed. The center is not origin but a biased form and is formed as a rotated elliptical shape. To compensate for this, first make an ellipse fitting like a red solid line. The fitted ellipse is able to know the information about the center point, the major axis and the minor axis as well as the angle of the major axis rotated from the x-axis. Use this information to perform hard and soft iron corrections.

First, if the hard iron correction is corrected, the center of the ellipse can be corrected to the origin.

Soft iron correction is performed by rotating the major axis of the ellipse to the x-axis by rotating the major axis of the ellipse, then fitting it to the actual magnetic field size, and then rotating it again to maintain the original angle. This results in a circle that is fitted with a yellow circle, and this process is performed on all raw data to produce a circular magnetic field measurement of purple dotted lines. This value is used to generate Heading information.

Heading can be obtained by applying the corrected magnetometer data to (2.36). The results are shown in Figure 28.

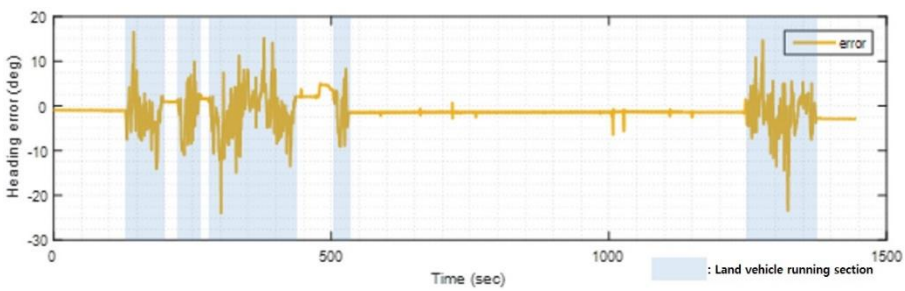

Figure 28. Magnetometer heading error plot.

Magnetometer is distorted due to the surrounding metallic or magnetic material, resulting in a large heading error. When installed in a land vehicle, errors occur due to surrounding vehicles, streetlights, and the like during driving. Therefore, error level is set by judging based on actual data. As a result, it is confirmed that a maximum error of 20 deg occurred in the section where the land vehicle driving, and a value within 10 deg when the vehicle stopped. Therefore, it is always applied to the system to have an error of 20deg to be applied to all the sections.

4.1.3 Extended Kalman Filter Tuning

System is tuned using the characteristics of actual DGPS data. Tuning is carried out considering two major considerations.

① **Considering the difference in DGPS position error level between driving and stopping.**

As a result of the analysis of the actual data position error, it is confirmed that the position error level of the land vehicle is stopped. (signal waiting, stopping, etc.)

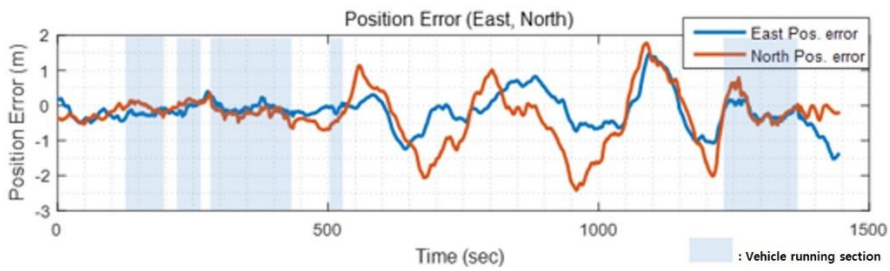

Figure 29. Actual data position error plot. (For tuning)

Therefore, we applied the differential position error level using the GPS speed provided by the receiver as the criterion for stopping. That is, we set the error of $0.7m \cdot 10 = 7m$ level when the speed is less than 1m / s and the error level of $0.7m$ when the speed is more than 1m/s.

$$\sigma_{Pos.GPS} = \begin{cases} 0.7m & (|V| > 1m/s) \\ 7m & (|V| \le 1m/s) \end{cases} \quad (4.16$$

Since there is no difference in the error level between the stopping and running sections, the speed is not set to be different.

② **Considering the positioning characteristics of GPS satellites.**

When GPS satellites are observed based on the local area (mid-latitude), the number of visible satellites in the north direction is insufficient (Figure 30), so that navigation errors in the north-south direction are larger than those in the east-west direction. Therefore, the position and velocity error level in the north-south direction is twice larger than that in the east-west direction.

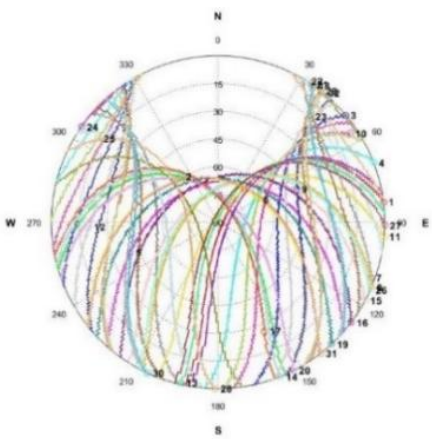

Figure 30. 24 hour skyplot of GPS satellite.

As a result, final measured DGPS position and velocity measurement error level are applied as shown in Table 10.

Table 10. DGPS position, velocity error tuning result.

Position	Driving	Stop	Velocity	All section
East	0.7m	7m	East	0.02m/s
North	1.4m	14m	North	0.04m/s

4.1.4 Heading alignment

Heading alignment should be performed when the experiment is conducted. Equipment that provides heading information in the configured system is provided by reference GPS receiver, low-cost GPS receiver, and magnetometer. However, when attaching these devices to the land vehicle, it is very difficult to attach them exactly to the heading direction of the land vehicle. Therefore, after attaching to the vehicle, alignment should be made to match the heading of the vehicle.

As shown in Figure 31, heading direction and the direction of the GPS velocity vector coincide when the land vehicle is running straight. Therefore, the alignment is performed using the fact that the heading generated at the GPS speed when the land vehicle is traveling straightly matches the heading of the land vehicle.

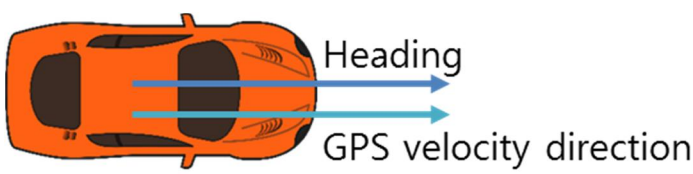

Figure 31. Heading alignment

4.2 Configure the experiment environment and scenario

Experimental experiments were carried out at the open area of Songdo area in Incheon to receive GPS information all the time. Data collection time is 3:10~33 pm on August 5th, 2016.

Satellite environment of the data gathering place is very good like the skyplot in Figure 32, and the visible satellite is observed in about 10 units.

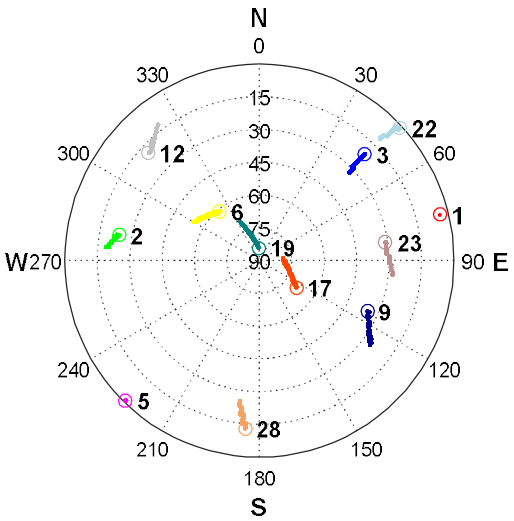

Figure 32. Visible satellite of the data collection site.

Experimental location and the land vehicle used in the experiment are shown in Figure 33 and the data collection is as shown in Figure 34.

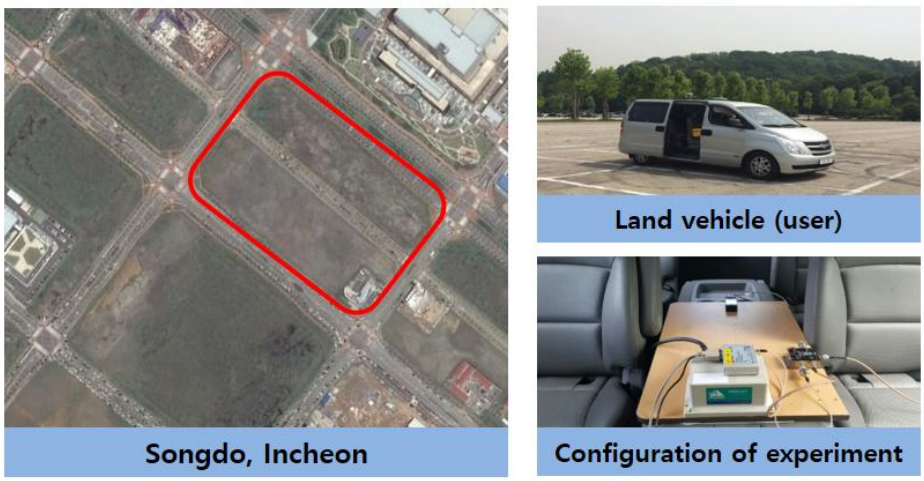

Figure 33. Place of experiment and user.

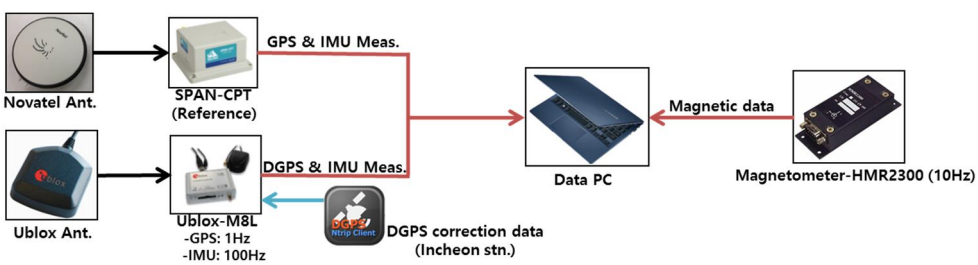

Figure 34. System configuration

An expensive GPS/INS receiver (SPAN-CPT) is installed for reference and provides GPS RTK and IMU measurements. In addition, low-cost GPS receiver (Ublox-M8L) to be used for the actual research uses a dedicated patch antenna. also, DGPS correction information is provided in real time through the NTRIP client, so that DGPS location and IMU measurements can be provided. Finally, magnetometer is installed to receive magnetic data using Honeywell's HMR-2300.

Actual data collection scenario is configured as shown in Figure 35.

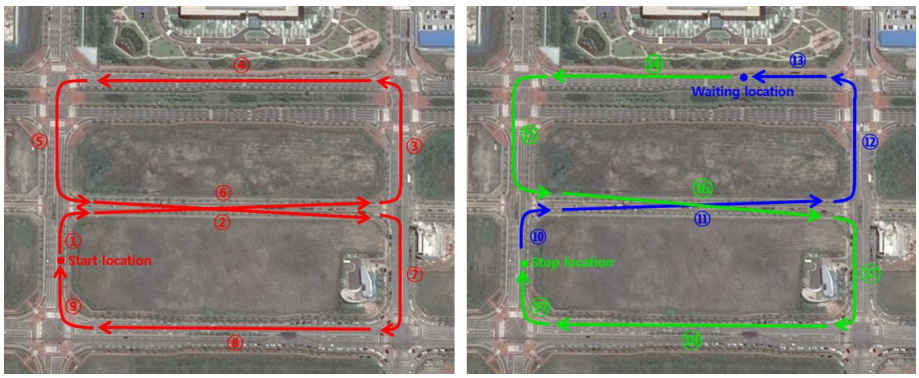

Figure 35. Data collection scenario

① Departs 1 minute from departure location. (①)

② 8-shape section 1 track drive. (②~⑨)

③ Drive to stop section. (⑩~⑫)

④ 10-minute stop from waiting location. (⑬)

⑤ Stop at stop location while moving 8-shape section. (⑭~⑲)

4.3 Actual experiment result

All the results of the actual experiment were analyzed by post-processing.

4.3.1 Compare results before and after considering gravity

Considering the characteristics of the actual data, the model of the IMU sensor is changed by the actual roll and pitch. And applied it to the system. In order to verify the performance of the new system, we analyzed the horizontal position error before and after applying the new model using the same actual experiment data.

Since the influence of the new sensor model is maximized when the attitude of the land vehicle changes, we analyze the horizontal position error for every corner section of the 8-shape trajectory. The results are shown in Figure 36, and the rms analysis is shown in Table 11. As a result, it is confirmed that the system using the new sensor model improved the horizontal position error of the corner section by about 13.6%.

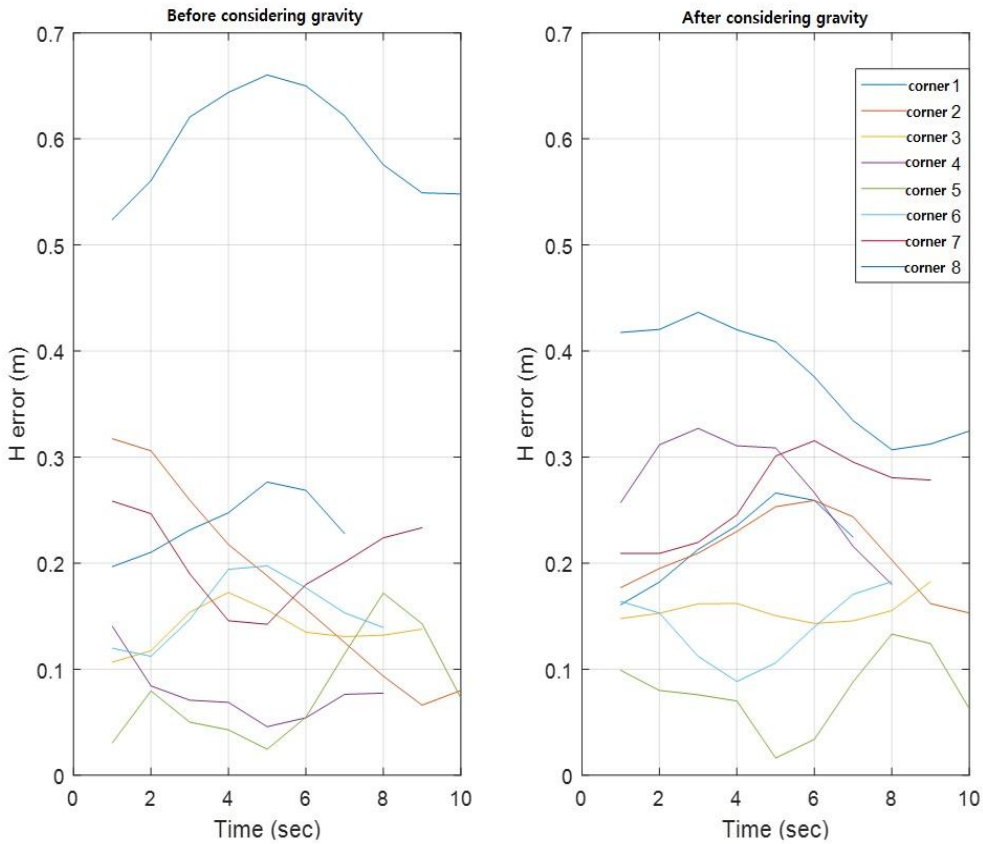

Figure 36. Comparison of horizontal position error plot before and after considering gravity at all corner.

Table 11. Comparison of horizontal position error rms result before and after considering gravity at all corner.

All turning section	Previous	Proposed
Horizontal position error rms	0.2723m	0.2353m

4.3.2 Analyzing the results of gravity considerations

4.3.2.1 East, North position error result

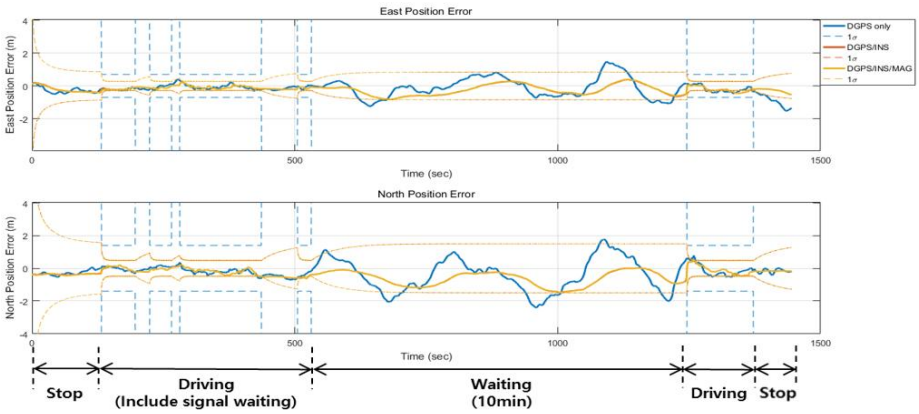

Figure 37. East, North position error plot.

Table 12. East position error rms result.

	DGPS only	DGPS/INS	DGPS/INS/Mag
East position error rms	0.517m	0.3292m	0.3282m
Improved accuracy (Compared to DGPS only)	-	36.3%	36.5%

Table 13. North position error rms result.

	DGPS only	DGPS/INS	DGPS/INS/Mag
North position error rms	0.798m	0.5804m	0.5808m
Improved accuracy (Compared to DGPS only)	-	27.3%	27.2%

The results of position error of East and North are summarized in Figure 37, Table 12, and Table 13. As a result, Positioning accuracy is improved by adding INS to DGPS only. When the magnetometer use additionally, it showed almost similar results in terms of position accuracy.

4.3.2.2 Horizontal position error result

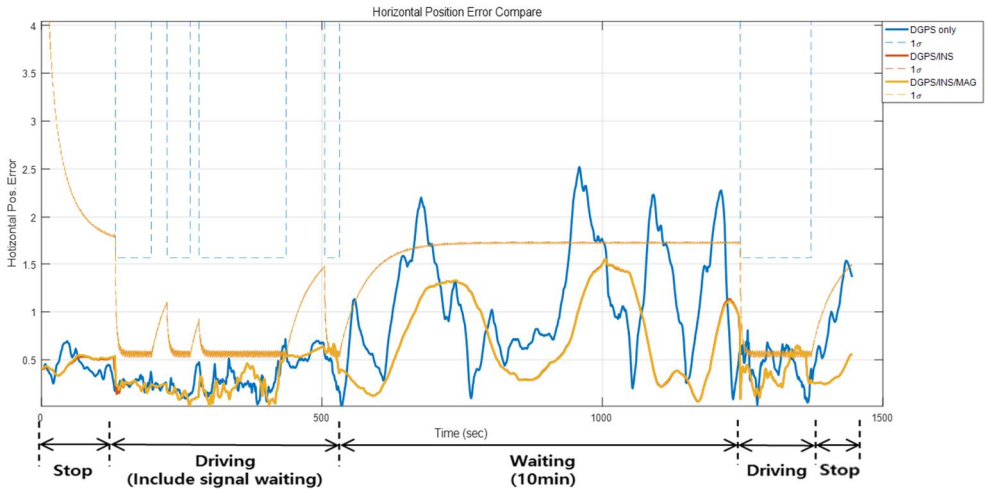

Figure 38. Horizontal position error plot.

Table 14. Horizontal position error rms.

	DGPS only	DGPS/INS	DGPS/INS/Mag
Horizontal position error rms	0.9512m	0.6673m	0.6671m
Improved accuracy (Compared to DGPS only)	-	29.8%	29.9%

The results of horizontal position error is smmarized in Figure 38 and Table 14. The results show that the horizontal position accuracy is improved by adding INS to DGPS only, and the horizontal position accuracy is almost similar when the magnetometer is additionally used.

4.3.2.3 Heading error result

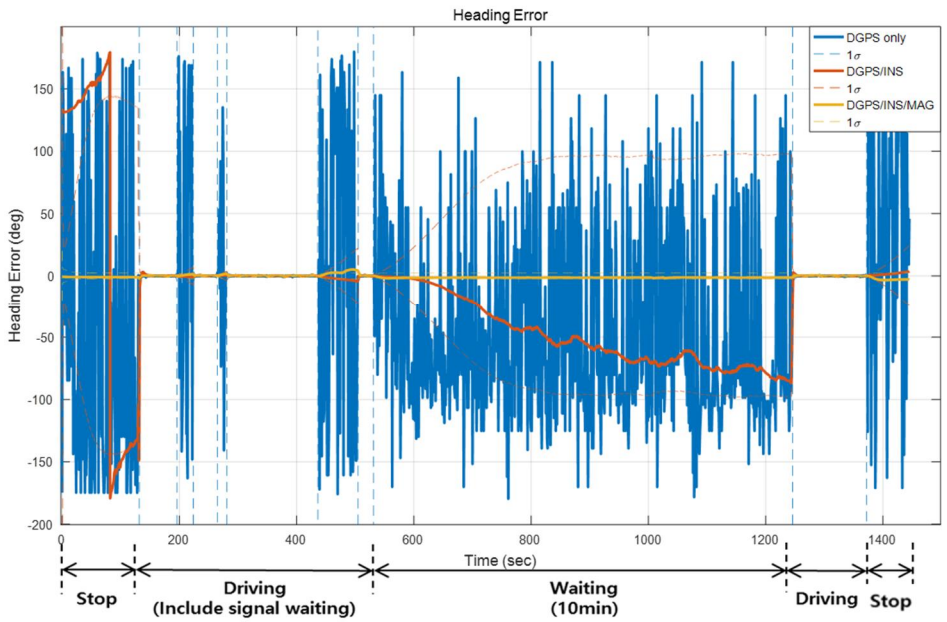

Figure 39. Heading error plot.

Heading error results are shown in Figure 39. The results show that DGPS only does not provide heading information for all section where the land vehicle is stop. In this case, if the INS is additionally used, gyroscope can be used to estimate a certain amount of time in the signal waiting period where the stop time is relatively short. However, If the stopping time is long, errors will diverge due to the limitation of gyroscope performance. However, this problem can be solved by adding a magnetometer and providing stable heading for all sections.

4.3.2.4 Bias error result

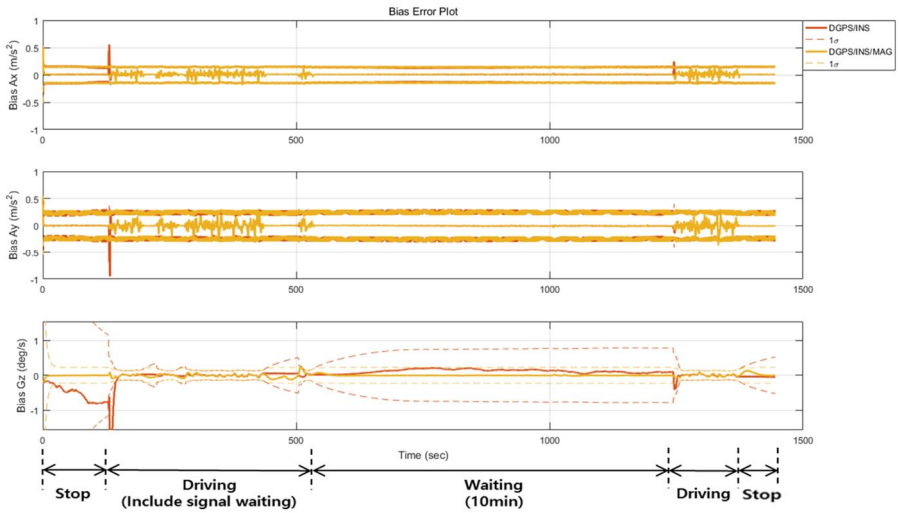

Figure 40. Bias error plot.

Bias error results are shown in Figure 40 As a result, it is confirmed that more stable bias estimation is possible by using magnetometer compared to DGPS/INS.

4.3.2.5 Sectional analysis result

① Waiting section analysis

Analysis is performed only for the section where the land vehicle stops for 10 minutes.

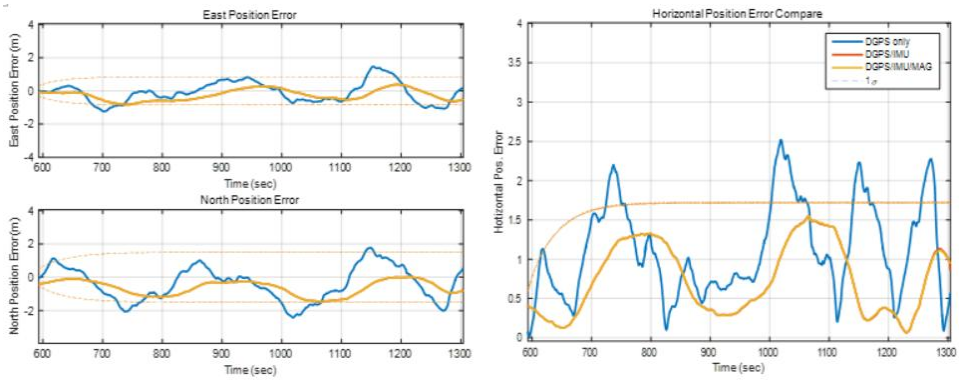

Figure 41. Position error plot. (Waiting section)

Table 15. Horizontal position error rms result. (Waiting section)

Waiting section	DGPS only	DGPS/INS	DGPS/INS/Mag
Horizontal position Error rms	1.260m	0.868m	0.867m
Improved accuracy (Compared to DGPS only)	-	31.1%	31.2%

Figure 41 and Table 15 summarize the results of the horizontal position error in the waiting section. As a result, the horizontal position accuracy is improved by 31.1% when INS is added to DGPS only, and the horizontal position accuracy is similar when the magnetometer is additionally used.

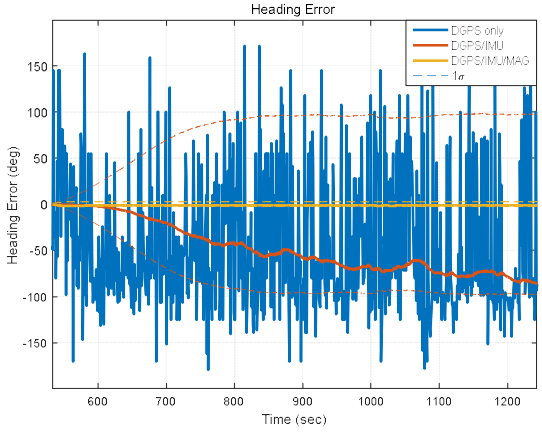

Figure 42. Heading error plot. (Waiting section)

Table 16. Heading error rms result. (Waiting section)

Waiting section	DGPS only	DGPS/INS	DGPS/INS/Mag
Heading error rms	-	55.1deg	1.4deg
Improved accuracy (Compared to DGPS/INS)	-	-	97.4%

The results of the heading error is summarized in Figure 42 and Table 16. As a result, DGPS only cannot continue to provide heading information because the land vehicle is stop. However, if INS is added, Heading cannot be provided for DGPS information, but it is estimated using gyroscope. However, it is confirmed that the error increased with time. If the magnetometer is added, the heading information can be always provided even during the stopping section, so that stable heading can be maintained at all times. As a result, it is confirmed that the accuracy of heading is improved by 97.4% compared to DGPS/INS.

② Driving section analysis

Analysis of the driving section is performed for the section where the land vehicle only drives without the signal waiting section.

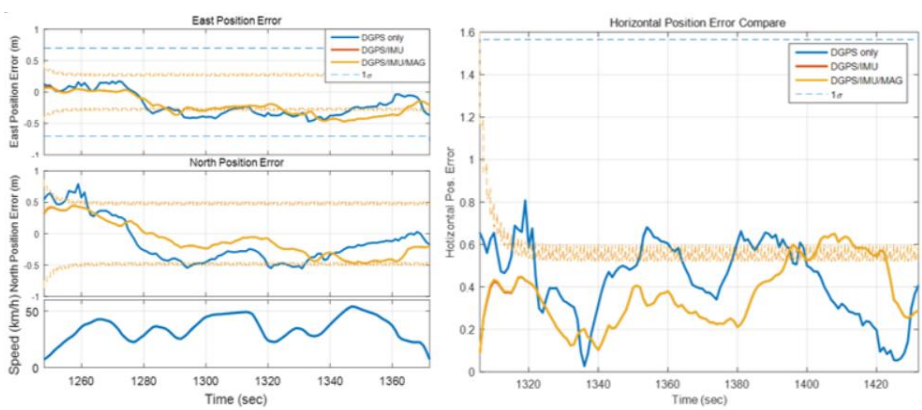

Figure 43. Position error plot. (Driving section)

Table 17. Position error rms result. (Driving section)

Driving section	DGPS only	DGPS/INS	DGPS/INS/Mag
Horizontal position Error rms	0.4670m	0.3977m	0.3984m
Improved accuracy (Compared to DGPS only)	-	14.8%	14.7%

Figure 43 and Table 17 summarize the results for the horizontal position error in the driving section. As a result, horizontal position accuracy is improved by 14.8% when INS is added to DGPS only, and horizontal position accuracy is similar when additional magnetometer is used.

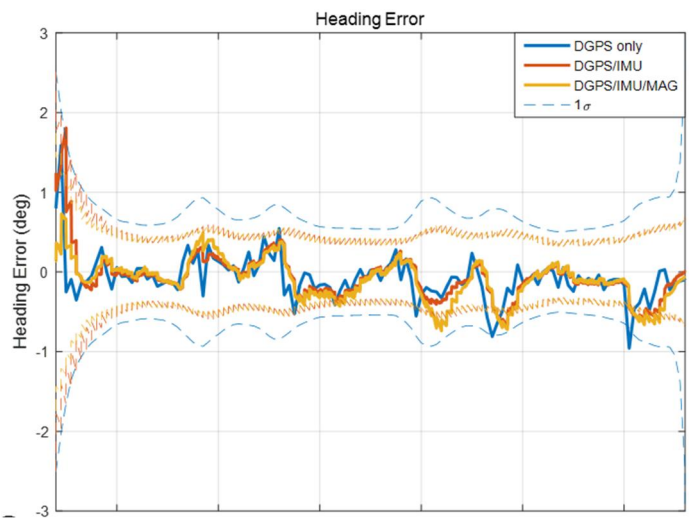

Figure 44. Heading error plot. (Driving section)

Table 18. Heading error rms result. (Driving section)

Driving section	DGPS only	DGPS/INS	DGPS/INS/Mag
Heading error rms	0.29deg	0.28deg	0.26deg
Improved accuracy (Compared to DGPS only)	-	3.4%	10.3%

Figure 44 and Table 18 summarize the heading errors in the driving section. Since the heading accuracy of DGPS only is basically very accurate, it can be seen that the addition of INS improves the accuracy but it improves marginally. In addition, even with the addition of a magnetometer, the accuracy is almost similar.

5. Conclusion and future work

In this paper, to develop a 2D DGPS/INS/Magnetometer combined navigation algorithm for land vehicle, Extended Kalman Filter is constructed by applying characteristics of land vehicle and measured values. In this case, it is possible to reduce the amount of computation by simplifying 2D in accordance with the characteristics of the land vehicle, and the system is constructed by improving the IMU sensor measurement modeling by grasping the actual land vehicle driving characteristics. In addition, by adding a magnetometer, it is possible to provide stable heading and ensure stability when heading information is provided when the land vehicle stops or runs at low speed, which is the limit of DGPS/INS. Also, system tuning is performed considering the dynamic characteristics of the DGPS measurements and satellite positioning characteristics.

Simulation used to determine if the system is defects, and to improve the performance by navigating. There is a performance enhancement through post-processing analysis by applying the system to actual land vehicle.

From the actual experimental results, it is confirmed that the horizontal position error result is improved about 13.6% on the rms basis before and after applying the IMU sensor measurement modeling. Actual experimental results show that the horizontal position error is 29.8% for DGPS/INS and 29.9% for DGPS/INS/Magnetometer compared to DGPS only. Heading error also shows that when the land vehicle is running, the heading accuracy of the DGPS is very high, so that the error remains small. However, when the land vehicle is stopped, the heading diverges from both the DGPS only and the DGPS/INS results. However, in the case of DGPS/INS/Magnetometer, it is confirmed that

stable heading is always provided in all sections including the stop section. As a result, the navigation performance is improved while considering practicality.

In the future research plan, the current research is based on the assumption that there is no change in the altitude of the vehicle, but research on upgrading the system so that it can be applied to various environments such as overpass and underground roads in actual road conditions will be needed. Finally, it will be useful if the system is systemized into a land vehicle and applied to unmanned vehicles and future-oriented safety and convenience devices.

6. References

[1] Korea Communications Agency, “미래사회를 준비하는 자율주행 ICT 기술동향”, 방송통신기술 이슈&전망 제 26 호, 2013.

[2] 송정훈, 서대화, “차량용 센서융합 정밀 측위 기술”, *한국통신학회지*, pp. 33-50, 2013.

[3] 박진원, 최계원, “차량정밀측위를 위한 복합 측위 기술 동향”, *한국전자통신학회 논문지*, pp. 139-144, 2016.

[4] Quan Zhang, “Algorithm Improvement of the Low-End GNSS/INS System for Land Vehicles Navigation”, Hindawi Publishing Corporation, Vol. 2013, p. 12, 2013.

[5] Cappelle, C., D. Pomorski, Y. Yang, “GPS/INS data fusion for land vehicle localization”, Proceedings of the IMACS Multi conference on Computational Engineering in Systems Applications, Beijing, China. Vol. 46. 2006.

[6] Sukkarieh, Salah, Eduardo Mario Nebot, “A high integrity IMU/GPS navigation loop for autonomous land vehicle applications”, *IEEE Transactions on Robotics and Automation*, pp.572-578, 1999.

[7] S. I. Jeon, “GPS-RTK Integration using In-flight calibration”, Master’s Thesis, Seoul National University, 2009.

[8] 김주원, 이동건, 이상선, “저가형 GPS/IMU 를 이용한 분산구조형태의 차량 위치 추정 알고리즘”, 한국통신학회 학술대회논문집, pp. 685-686, 2015.

[9] 이정환, 김한실, “GPS/INS 센서 융합을 이용한 고정밀 위치 추정에 관한 연구”, *전자공학회논문지*, pp. 159-166, 2012.

[10] 김도윤, 박현근, “관성 센서와 GPS 약결합을 통한 GPS 음영지역에서 차량 위치 추정”, *2011 대한전기학회 하계학술대회 논문집*, pp. 1942-1943, 2011.

[11] O.Maklouf, Ahmed Abdulla, “1G2A IMU/GPS Integration Algorithm for Land Vehicle Navigation”, World Academy of Science, Engineering and Technology, Vol. 8, No. 3, 2014.

[12] 송종화, 김광훈, 지규인, 이연석, “차량 움직임 정보를 이용한 GPS/DR 차량항법시스템 성능향상”, 로봇학회 논문지, pp. 55-63, 2010.

[13] Tan, Han-Shue, and Jihua Huang, “DGPS-based vehicle-to-vehicle cooperative collision warning: Engineering feasibility viewpoints”, *IEEE Transactions on Intelligent Transportation Systems*, pp.415-428, 2006.

[14] Y. M. Han, “Relative Position Estimation of Miniature Vehicles using GPS/MEMS IMU”, Master’s Thesis, Seoul National University, 2012.

[15] Liu, Cheng-Yueh, et al., “Performance evaluation of real-time MEMS INS/GPS integration with ZUPT/ZIHR/NHC for land navigation”, *ITS Telecommunications (ITST), 2012 12th International Conference on*. IEEE, 2012.

[16] Kubo, Yukihiro, Kindo, Tsuyoshi, Ito, Akihiko, Sugimoto, Sueo, “DGPS/INS/Wheel Sensor Integration for High Accuracy Land-Vehicle Positioning”, Proceedings of the 12th International Technical Meeting of the Satellite Division of the Institute of Navigation (ION GPS 1999), Nashville, TN, September, pp. 555-564, 1999.

[17] Dumitrache, A., et al., “Hybridized GPS/DR positioning system with unknown initial heading for land vehicles”, *11th International IEEE Conference on Intelligent Transportation Systems*. IEEE, 2008.

[18] Rezaei, Shahram, Raja Sengupta, “Kalman filter-based integration of DGPS and vehicle sensors for localization”, *IEEE Transactions on Control Systems Technology*, pp. 1080-1088, 2007.

[19] Hang Guo, “Kalman filtering for GPS/magnetometer integrated navigation system”, Advances in Space Research, 2010.

[20] J. M. Kim, “Development of GPS and Magnetometer Aided Inertial Navigation System”, Master’s Thesis, Inha University, 2007.

[21] 이승준, et al., “지자기 센서의 결합 시기에 따른 GPS/INS/지자기계 결합항법 시스템의 성능 분석”, *한국항공우주학회 2013 년도 춘계학술대회*, pp. 614-618, 2013.

[22] 신광수, 안병규, 임종석, “지자기 센서를 통합한 항법 필터 설계”, *한국정보과학회 학술발표논문집*, pp. 1576-1578, 2015.

[23] Gao, Shesheng, et al., “Multi-sensor optimal data fusion for INS/GPS/SAR integrated navigation system”, *Aerospace Science and Technology*, pp. 232-237, 2009.

[24] E. H. Shin, “Accuracy Improvement of Low Cost INS/GPS for Land Applications”, Master’s Thesis, Calgary University, 2001.

[25] Elliot D.Keplan, “Understanding GPS Principles and Application”, Artech House, 2005.

[26] Parkinson B, “Global Positioning System; Theory and Applications I”, Progress in Astronautics and Aeronautics, 1996.

[27] Parkinson B, “Global Positioning System; Theory and Applications II”, Progress in Astronautics and Aeronautics, 1996.

[28] P. Misra and P. Enge., “Global Positioning System-Signals, Measurements, and Performance”, Ganga-Jamura Press, 2001.

[29] David H. Titterton and John L. Weston, “Strapdown Inertial Navigation Technology”, 2nd ed., The Institution of Electrical Engineers, 2004.

[30] Stockwell, Walter, “Bias stability measurement: Allan variance”, *Crossbow Technology, Inc., Tech. Rep,* 2004.

[31] K. H. Han, “On Integration of GPS/INS”, Master’s Thesis, Seoul National University, 2001.

[32] Nguyen, Vinh Hao, “Loosely coupled GPS/INS integration with Kalman filtering for land vehicle applications”, *Control, Automation and Information Sciences (ICCAIS), International Conference on*. IEEE, 2012.

[33] R. G. Brown, Patrick Y. C. Hwang, “Introduction to Random Signals and Applied Kalman Filtering”, WILEY, 4th ed., 2012.

초 록

본 논문에서는 저가형 GPS(Global Positioning System) 수신기, MEMS IMU(Inertial Measurement Unit), Magnetometer 를 이용한 차량의 항법 측위 성능 향상에 관한 알고리즘을 제안한다. Stand-alone GPS 의 성능을 향상시키고자 사용자 주변에 있는 기준국의 보정정보를 이용하는 DGPS(Differential GPS)를 이용하였다. 또한, 차량용 시스템을 개발하기 위해서 차량의 동적인 특성을 기반으로 시스템을 단순화하여 2D 을 적용하였고, 단순화 과정으로 인해 발생하는 오차를 최소화하고자 실제 차량 주행 특성을 파악하여 IMU 센서 측정치 모델링을 개선하여 결과적으로는 시스템은 단순화하면서도 항법 해 성능은 유지할 수 있도록 하였다. 그리고 GPS/INS 의 한계점인 차량이 정지하거나 저속으로 주행할 경우 Heading 정보가 발산하는 것을 Magnetometer 를 추가함으로써 보완할 수 있도록 하여 최종적으로는 DGPS/INS/Magnetometer 결합 EKF(Extended Kalman Filter)를 구성하여 항법 해 성능 향상을 도모하였다.

구성한 차량용 DGPS/INS/Magnetometer 결합 EKF 시스템을 검증하고자 simulation 을 통해 이상 유무 판단 및 항법 해 성능

향상이 가능함을 검증하였고, 실제 차량에 시스템을 적용하여 후처리 분석을 통한 항법 해 성능 향상을 확인하였다.

주요어: 차량, GPS/INS 통합, 지자기 센서, 칼만 필터

학번: 2015-20762